ARTICLES

Scaled energy (z) distributions of charged hadrons observed in deep-inelastic muon scattering at 490 GeV from xenon and deuterium targets

M. R. Adams,[6] S. Aïd,[9,a] P. L. Anthony,[10,b] M. D. Baker,[10] J. Bartlett,[4] A. A. Bhatti,[13,c] H. M. Braun,[14] W. Busza,[10] T. Carroll,[6] J. M. Conrad,[5,d] G. Coutrakon,[4,e] R. Davisson,[13] I. Derado,[11] S. K. Dhawan,[15] W. Dougherty,[13] T. Dreyer,[1,f] K. Dziunikowska,[8] V. Eckardt,[11] U. Ecker,[14,a] M. Erdmann,[1,g] A. Eskreys,[7] J. Figiel,[7] H. J. Gebauer,[11] D. F. Geesaman,[2] R. Gilman,[2,h] M. C. Green,[2,i] J. Haas,[1] C. Halliwell,[6] J. Hanlon,[4] D. Hantke,[11] V. W. Hughes,[15] H. E. Jackson,[2] D. E. Jaffe,[6,j] G. Jancso,[11] D. M. Jansen,[13,k] S. Kaufman,[2] R. D. Kennedy,[3,h] T. Kirk,[4,l] H. G. E. Kobrak,[3] S. Krzywdzinski,[4] S. Kunori,[9] J. J. Lord,[13] H. J. Lubatti,[13] D. McLeod,[6] S. Magill,[6,m] P. Malecki,[7] A. Manz,[11] H. Melanson,[4] D. G. Michael,[5,n] W. Mohr,[1] H. E. Montgomery,[4] J. G. Morfin,[4] R. B. Nickerson,[5,o] S. O'Day,[9,p] K. Olkiewicz,[7] L. Osborne,[10] V. Papavassiliou,[15,m] B. Pawlik,[7] F. M. Pipkin,[5,q] E. J. Ramberg,[9,p] A. Röser,[14,r] J. J. Ryan,[10,s] A. Salvarani[3,t] H. Schellman[12], M. Schmitt,[5,u] N. Schmitz,[11] K. P. Schüler,[15,l] H. J. Seyerlein,[11] A. Skuja,[9] G. A. Snow,[9] S. Söldner-Rembold,[11] P. H. Steinberg,[9,q] H. E. Stier,[1,q] P. Stopa,[7] R. A. Swanson,[3] R. Talaga,[9,m] S. Tentindo-Repond,[2,v] H. J. Trost,[2,w] H. Venkataramania,[15] M. Vidal,[11] M. Wilhelm,[1] J. Wilkes,[13] Richard Wilson,[5] W. Wittek,[11] S. A. Wolbers,[4] and T. Zhao[13]

[1] *Albert-Ludwigs-Universität, D-7800 Freiburg i. Br., Germany*
[2] *Argonne National Laboratory, Argonne Illinois 60439*
[3] *University of California, San Diego, California 92093*
[4] *Fermi National Accelerator Laboratory, Batavia, Illinois 60510*
[5] *Harvard University, Cambridge, Massachusetts 02138*
[6] *University of Illinois, Chicago, Illinois 60680*
[7] *Institute for Nuclear Physics, Krakow, Poland*
[8] *Institute for Nuclear Physics, Academy of Mining and Metallurgy, Krakow, Poland*
[9] *University of Maryland, College Park, Maryland 20742*
[10] *Massachusetts Institute of Technology, Cambridge, Massachusetts 02139*
[11] *Max-Planck-Institut für Physik, 80805 Munich, Germany*
[12] *Northwestern University, Evanston, Illinois 60208*
[13] *University of Washington, Seattle, Washington 98195*
[14] *University of Wuppertal, D-5600 Wuppertal, Germany*
[15] *Yale University, New Haven, Connecticut 06511*

(Received 4 August 1993)

Fermilab Experiment-665 measured deep-inelastic scattering of 490 GeV muons off deuterium and xenon targets. Events were selected with a range of energy exchange ν from 100 GeV to 500 GeV

[a]Present address: Büro Schellmann, Rabenhorst 29, Hamburg 65, Germany.
[b]Present address: Lawrence Livermore National Laboratory, Livermore, CA 94550.
[c]Present address: The Rockefeller University, New York, NY 10021.
[d]Present address: Columbia University, New York, New York 10027.
[e]Present address: Loma Linda University Medical Center, Loma Linda, CA 92350.
[f]Present address: RACOS, Maybachstr. 3, D-7750 Konstanz, Germany.
[g]Present address: DESY, Notkestr. 85, 2000 Hamburg, Germany.
[h]Present address: Rutgers University, Piscataway, NJ 08855.
[i]Present address: LeCroy Research Systems, Spring Valley, NY 10977.
[j]Present address: SCRI, Florida State University, Tallahassee, FL 32306.
[k]Present address: Los Alamos National Laboratory, Los Alamos, New Mexico 87545.
[l]Present address: SSC Laboratory, Dallas, TX 75237.
[m]Present address: Argonne National Laboratory, Argonne, IL 60439.
[n]Present address: California Institute of Technology, Pasadena, California 91125.
[o]Present address: Oxford University, Oxford, OX1 3NP United Kingdom.
[p]Present address: Fermi National Accelerator Laboratory, Batavia, Illinois 60510.
[q]Deceased.
[r]Present address: Ruhruniversität Bochum, D-4630 Bochum 1, Germany.
[s]Corresponding author: RM 24-508, Massachusetts Institute of Technology, Cambridge, MA 02139. Electronic address: jryan@mitlns.mit.edu
[t]Present address: AT&T, Bell Labs. 2000 North Naperville Road, Naperville, Illinois 60555.
[u]Present address: University of Wisconsin, Madison, Wisconsin 53706.
[v]Present address: Northern Illinois University, Dekalb, Illinois 60115.
[w]Present address: Texas A&M University, College Station, Texas 77843.

and with large ranges of Q^2 and x_{Bj}: 0.1 GeV$^2/c^2 < Q^2 <$ 150 GeV$^2/c^2$ and $0.001 < x_{Bj} < 0.5$. The fractional energy (z) distributions of forward-produced hadrons from the two targets have been compared as a function of the kinematics of the scattering; specifically, the kinematic region of "shadowing" has been compared to that of nonshadowing. The dependence of the distributions upon the *order* of the hadrons, determined by the fractional energies, has been examined as well; a strong degree of similarity has been observed in the shapes of the distributions of the different order hadrons. These z distributions, however, show no nuclear dependence, even in the kinematic region of shadowing.

PACS number(s): 13.60.Le, 13.10.+q, 25.30.Mr

I. INTRODUCTION

A. Motivation

Fermilab Experiment-665 was constructed to measure deep-inelastic muon scattering; the spectrometer has been described in Ref. [1]. This analysis concentrates on the distributions of the final state hadrons produced in these scattering events. It was based on the data from the first period of running, in 1987. Details of the data set and the analysis chain may be found in Ref. [2].

E665 had the advantage of very high incident muon energy, 490 GeV, which allowed large values of energy exchange ν, and hence very small x_{Bj} values (the kinematic variables are described in Sec. II A). In addition, acceptance down to small muon scattering angles (1 mrad) allowed for an examination of the *shadowing* (see Sec. II D) effect over large ranges of the kinematic variables ν, Q^2, and x_{Bj}:

$$100 \text{ GeV} < \nu < 500 \text{ GeV},$$

$$0.1 \text{ GeV}^2/c^2 < Q^2 < 150 \text{ GeV}^2/c^2,$$

and

$$0.001 < x_{Bj} < 0.5.$$

In this analysis we examine the final state hadron distributions as functions of the hadron fractional energy (z). The events analyzed were selected from the xenon and deuterium target samples. We compare our z distributions from deuterium to those from the European muon collaboration (EMC) [3] and CHIO [4]. We then examine the dependences of our distributions upon the event kinematics, paying particular attention to comparing the distributions from a "simple" target, deuterium, to those from a nuclear target, xenon.

In the kinematic regime of shadowing, the inclusive inelastic cross section on a nuclear target exhibits a depletion at low x_{Bj} relative to a "simple" proton-neutron isoscalar target [5,6]. A similar nuclear dependence of the cross section has been seen in hadron-nuclear [7] and photon-nuclear collisions [8]. In addition, in the hadron-nuclear interactions the scaled energy distributions of the final state hadrons have displayed a corresponding nuclear dependence; nuclear dependence of the final state hadrons from the nondiffractive channel of real photoproduction has not been published. In inelastic scattering in the shadowing regime, the virtual photon may be "nearly" real. Since the cross section for muon scattering from xenon exhibits a depletion in this kinematic region, the final state hadrons may show a corresponding nuclear dependence; hadron studies have not been presented in this kinematic region of inelastic scattering before this experiment. We compare our z distributions from the regime of shadowing to that of nonshadowing; it is of special interest that these comparisons show no nuclear dependence.

In a separate publication [9], we have compared the multiplicity distributions and other properties of the final state hadrons of xenon and deuterium. That analysis was based on a streamer chamber data sample, with a different kinematic range than this analysis; it includes an examination of the backward hemisphere. The physics conclusions of these two analyses are consistent for the forward produced hadrons.

B. Overview

Before presenting our results, we review some aspects of deep-inelastic muon scattering. In Sec. II A, we cover the standard formalism of the interaction kinematics. In Sec. II B we define the variables used to describe the final state hadrons. In Sec. II D we discuss the effect of shadowing, and finally, in Sec. II E, we discuss expectations for nuclear dependence of the hadronic final states.

In Sec. III we examine the z distributions from xenon and deuterium. We begin by comparing our deuterium data to data from previous experiments in Sec. III A. Then, in Sec. III B, we compare our z distributions from both targets in both regimes, shadowing and nonshadowing. The effects of rescattering in the targets are considered in Sec. IV, and limits on nuclear effects on the final state hadrons are presented in Sec. V.

We also examine the event structure for the two kinematic regions, from both targets, by comparing the z distributions for hadrons of different order, where the order is determined by the fractional energy; this is presented in Sec. VI. The removal of a kinematic constraint is accomplished by rescaling the fractional energies in Sec. VI C. The conclusions from our analysis are presented in Sec. VII.

We have included Appendix A, in which we present some detailed examinations of several effects that could have biased the results. In Appendix A 1 we summarize the systematic error on the z distributions, and the resolution on the energy fraction z is discussed in Appendix A 2. We discuss the selection criteria for events

to be included in the final sample and the quality requirements imposed on the tracks of these events. Several of the "cuts" were based on a particular kinematic variable; since the kinematic variables are correlated, a given cut affects several variables. Hence, the final kinematic space of the data sample is described in detail in Appendix A 3.

Corrections for contamination by radiative processes have *not* been applied in this analysis, unlike previous analyses; instead, we have employed information from our electromagnetic calorimeter to reduce the contamination of these radiative processes, before examining the hadron distributions. Details of this procedure are presented in Appendix A 5.

In Appendix A 6, we cover the method employed to correct the data for acceptance and reconstruction. Monte Carlo events, based on LUND [10], were used only to simulate the effects of acceptance on the distributions. They were not considered as a means of evaluating the physics of the distributions.

The distributions of the final state hadrons have been normalized to the number of scattered muons. The data were collected based upon two different triggers; the validity of merging the two samples depended upon the demonstration that, for similar kinematics, the two triggers did not bias the hadron distributions. This demonstration is located in Appendix A 7.

In Appendix B, we have tabulated our data from those plots which present our results; the errors associated with each value are included.

C. Conventions

Throughout this paper the presentation of the figures adheres to certain conventions. All vertical error bars represent only the statistical errors; horizontal error bars indicate one-half the bin-width and no bin-centering correction has been applied. Unless explicitly stated otherwise, all hadron distributions have been corrected for acceptance but not for target length effects, which are discussed explicitly. The event distributions in the muon variables have *not* been corrected for either triggering or detector acceptance because they indicate the actual data samples used in the hadron analysis and, hence, the space of the total cross section which has been probed.

II. DEEP-INELASTIC MUON SCATTERING

A. Kinematics

The deep-inelastic muon-nucleon scattering process involves the transfer of energy and momentum from the muon to the target through an electroweak interaction. In the Born approximation, this is described as the transfer of a single boson. In our kinematic regime, we need only consider an electromagnetic interaction. The Feynman graph of single-photon exchange is shown in Fig. 1. The incoming muon has four-momentum k, and the outgoing muon, scattered through a lab angle θ, has four-momentum k'. The initial four-momentum of the target

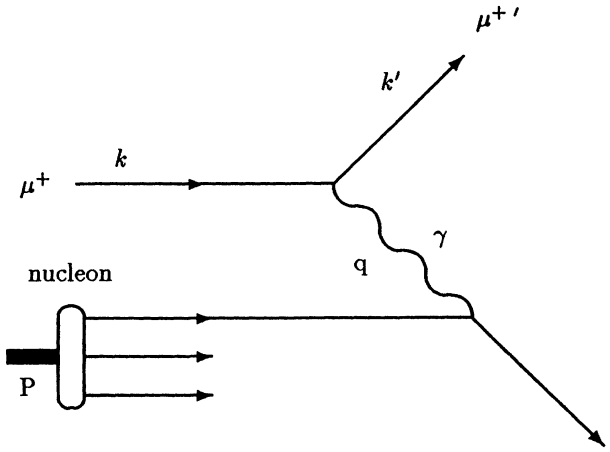

FIG. 1. Feynman graph of single-photon exchange.

is defined to be P, and the four-momentum transferred in the interaction is defined as $q = k - k'$. Since the photon is "spacelike," the square of the four-momentum transfer is negative: $q^2 < 0$; hence, it is customary to define the positive quantity $Q^2 \equiv -q^2$. In the laboratory system the target nucleon is assumed to be initially at rest, so $P = (M; 0, 0, 0)$, where M is the nucleon mass; we are ignoring the effects of Fermi motion. With the energies of the incident and outgoing muons defined as E and E', respectively, the energy transferred in this system is defined as $\nu \equiv E - E'$, and thus $q = (\nu; \bar{k} - \bar{k}')$. The expression for Q^2 is then

$$Q^2 = -2m_\mu^2 + 2EE' - 2|\bar{k}||\bar{k}'|\cos\theta. \tag{1}$$

Since the interaction is inelastic, energy is contributed to the breakup of the target, and a parameter is required to describe the relative inelasticity of the interaction. It is natural to employ the Bjorken-scaling variable to express this inelasticity:

$$x_{\mathrm{Bj}} \equiv \frac{Q^2}{2M\nu}, \tag{2}$$

which takes values in the interval (0,1), with $x_{\mathrm{Bj}} = 1$ for elastic scattering from a nucleon at rest. In the quark parton model [11], x_{Bj} is considered the fraction of momentum of the nucleon carried by the parton. The invariant mass of the final hadronic state is W; it includes the amount of energy absorbed into the struck-nucleon system. With this definition of W, the square of the four-momentum transfer can be arranged as the sum of a kinetic term and a mass term:

$$Q^2 = 2M\nu + (M^2 - W^2). \tag{3}$$

Another kinematic variable frequently used is the scaled-energy transfer: $y = \nu/E$. The important consideration here is that, for a given beam energy, there are two parameters needed to describe the kinematics of the scatter.

B. Hadron variables

In deep-inelastic scattering the trajectories of the primary hadrons can be expressed relative to the primary event vertex and the direction of the virtual photon, which are defined by the muon scattering kinematics. With the assumption of a particular mass, a typical choice of the three variables needed to describe the hadrons would be the longitudinal momentum relative to the event axis, $P_{\|}$, the transverse momentum P_t, and the azimuthal angle about the virtual photon axis, ϕ. One could choose the hadron total momentum or the energy instead of $P_{\|}$. When examining the hadron distributions as a function of one of these variables, one integrates over some range of the other two.

The energy available for distribution among the final state particles varies from event to event, so the momenta of the hadrons will depend on the event kinematics. Empirically, it has been possible to scale-out this dependence on the available energy by defining the Lorentz invariant quantity z:

$$z \equiv \frac{P_{\text{target}} \cdot P_{\text{hadron}}}{P_{\text{target}} \cdot q}, \tag{4}$$

where P_{target} is the four-momentum of the target, P_{hadron} is the four-momentum of the hadron, and q is the four-momentum transferred in the interaction. In the lab frame, z reduces to the ratio of the hadron energy over the energy transfer in the event: $z = E_h/\nu$, where E_h is the hadron energy. In this analysis, we have assumed a pion mass for all particles in calculating E_h. The Feynman scaling variable x_F is another frequently chosen method of scaling the momenta of particles:

$$x_F \equiv \frac{P_{\|}^{\text{c.m.}}}{P_{\|\text{max}}^{\text{c.m.}}} \approx \frac{P_{\|}^{\text{c.m.}}}{W/2}, \tag{5}$$

where $P_{\|\text{max}}^{\text{c.m.}}$ is the maximum possible longitudinal momentum in the center-of-mass system, which is well approximated by half the available energy. For the energies transferred in Experiment-665, the two variables x_F and z are equivalent for high-momentum particles: when x_F and z are greater than about 0.15. In this analysis, we will only discuss the energy fraction z.

We have also used information regarding the *ordering* of the particles in terms of their energy fractions z (Ref. [2]). The particle with the highest z was referenced as the *fastest* particle. Similarly, the next highest-z particle was called the *second fastest*, and the third highest-z particle was called the *third fastest*. This is the same terminology used by Feynman and Field [12]; they discuss *ordering* in energy as distinct from *ranking* in the fragmentation chain, which is not directly observable. We will consider only the experimental ordering in z. This ordering involved only charged particles, so there was some "shuffling up" of charged particles in the ordering, as their preceding neutral sisters were missed.

We have defined an additional variable, which we have called the rescaled z; this quantity is the energy of each particle scaled to the energy available to that particle, working down from the most energetic. Again, in calculating the energy available to a hadron, we considered only observed charged particles. The rescaled-z values of the second and third fastest particles are defined as

$$\text{Rescaled } z_2 \equiv \frac{P_{\text{nucleon}} \cdot P_2}{P_{\text{nucleon}} \cdot (q - P_1)} \tag{6}$$

$$\longrightarrow \left.\frac{E_2}{\nu - E_1}\right|_{\text{lab frame}}, \tag{7}$$

and

$$\text{Rescaled } z_3 \equiv \frac{P_{\text{nucleon}} \cdot P_3}{P_{\text{nucleon}} \cdot (q - P_1 - P_2)} \tag{8}$$

$$\longrightarrow \left.\frac{E_3}{\nu - E_1 - E_2}\right|_{\text{labframe}}, \tag{9}$$

where E_i is the energy and P_i is the four-momentum of the hadron of order i.

C. Factorization

The differential rate of production of hadrons depends, in principle, upon the event kinematics as well as the hadron kinematics. What we measure is the number of hadrons, N_h, produced in an interval dz of the energy fraction, integrated over a range of the other four variables:

$$\frac{dN_h}{dz} = \int\int\int\int \frac{d^5N_h}{dx_{\text{Bj}}\, dQ^2\, dz\, dP_t^2\, d\phi}\, dx_{\text{Bj}}\, dQ^2\, dP_t^2\, d\phi. \tag{10}$$

In the same range of the two event kinematic variables x_{Bj} and Q^2, we also measure the number of events, or scattered muons:

$$N_\mu = \int\int \frac{d^2N_\mu}{dx_{\text{Bj}}\, dQ^2}\, dx_{\text{Bj}}\, dQ^2. \tag{11}$$

By normalizing the number of hadrons per interval dz, Eq. (10), to the number of scatters, Eq. (11), we obtain the mean number of hadrons per event produced in the interval dz, which is a differential multiplicity distribution:

$$D(z) \equiv \frac{1}{N_\mu}\frac{dN_h}{dz}. \tag{12}$$

In principle, this function $D(z)$ could depend upon the specific range of the event kinematic variables x_{Bj} and Q^2 over which the integration was performed. Empirically, however, hadrons have shown only weak dependences on event kinematics, after scaling the hadron energies. Neglecting these weak dependences, we can factorize the production rate into the product of two independent rates:

$$\frac{d^5N_h}{dx_{\text{Bj}}\, dQ^2\, dz\, dP_t^2\, d\phi} = \frac{d^2N_\mu}{dx_{\text{Bj}}\, dQ^2}\frac{d^3N_H}{dz\, dP_t^2\, d\phi}, \tag{13}$$

where N_H is the mean number of hadrons produced in an event. This approximation is called *factorization*. The rationale for this behavior is that the scattering of the muon occurs on a much shorter time scale than that of

the target breakup and the formation of the final state hadrons, and, hence, the scattering of the muon can be considered independently from the breakup of the target.

While the approximation holds, the two factors of Eq. (13) can be integrated over their variables independently. This allows us to interpret $D(z)$ of Eq. (12) as a function of a single variable, with no dependence upon the scattering rate or the event kinematics, as a *fragmentation function*:

$$D(z) = \int\int \frac{d^3N_H}{dz\, dP_t^2\, d\phi}\, dP_t^2\, d\phi. \tag{14}$$

The validity of the factorization approximation for a specific range of kinematics can be tested empirically by examining the residual dependence of the hadron distributions upon the event kinematics. We inspect this aspect of our data for the z distributions.

D. Shadowing

Deep-inelastic scattering off nuclear targets has been compared to that off "nucleon" targets of hydrogen and deuterium. The per-nucleon cross section for a nuclear target differs from that for a hydrogen or deuterium target as a function of the scattering kinematics. There have been several effects seen as a function of the Bjorken scaling variable $x_{\rm Bj}$; there is an enhancement at very high $x_{\rm Bj}$ ($0.6 < x_{\rm Bj} < 1$), a reduction of cross section at mid-$x_{\rm Bj}$ ($0.3 < x_{\rm Bj} < 0.6$), an enhancement at $x_{\rm Bj} \sim 0.1$, and another reduction at very low $x_{\rm Bj}$ ($x_{\rm Bj} < 0.01$). These are associated with the effects of Fermi motion, the "EMC effect" [13], antishadowing [5], and shadowing [5], respectively. Of primary interest in this analysis is the effect of shadowing.

Shadowing is an effect which has been seen in hadron-nuclear scattering; the strong nature of the interaction is such that the scattering tends to occur very near the surface of the target nucleus before the incident hadron can traverse the nuclear material to reach the more downstream parts. Thus, the upstream part of the nucleus occults or "shadows" the downstream part. The cross section for the interaction depends on the target size as a function of the surface area and not the volume of material. This leads to a dependence closer to $A^{2/3}$ rather than to A^1, where A is the atomic weight of the nuclear target.

This effect has also been seen in real photon absorption on nuclei. The increase in cross section is approximately proportional to the area of the target nucleus and not the volume, and the relative cross section per target nucleon decreases as the A of the target nuclei is increased; empirically, the photoproduction dependence is roughly $A^{0.9}/A$. This has been described traditionally by vector meson dominance [8]. The photon can transmute itself into a virtual meson, which must have the same quantum numbers as the photon and hence must be spin-1: a vector meson. The lightest of these is the ρ^0 meson, which forms the basis of this description. In generalized vector meson dominance [8] the interaction must be summed over all possible vector mesons and the interference graphs as well, which correspond to off-diagonal elements of the scattering matrix. These off-diagonal elements of generalized vector meson dominance cancel the strong dependence of the process on Q^2 which exists in the simple ρ meson dominance picture.

Attempts also have been made to describe nuclear effects based on the parton picture. The Altarelli-Parisi equations have defined the basis of a popular description of partonic distributions within the framework of the theory of *quantum chromodynamics* (QCD). Based on the renormalization group equation and operator product expansion and on a QCD-inspired Lagrangian, they describe the makeup of a nucleon in terms of distributions of quarks (both valence and sea) and gluons. The authors developed functions to describe the interactions between the partons; these were called *splitting functions* because they involved the emission of partons (both quarks and gluons) from other partons (both quarks and gluons) [14]. The approach of Ref. [15] described nucleon structure not in terms of partons but in terms of emission and reabsorption of virtual mesons, nucleons, and antinucleons.

In more recent work [16–18] on the parton description, another set of functions was added which describes the process of recombining partons; this creates a more thorough characterization of the interactions between the partons. Particular attention was paid to the recombination of partons from neighboring nucleons in nuclei. As the fraction of nucleonic momentum carried by a parton, x, becomes small, the localization of the parton must become less precise, so these "wee-x" partons of a nucleon will overlap spatially with those of neighboring nucleons in a nucleus. The valence quarks will not stray far from the valence domain of 1 fm, but these wee-x partons may be located more than 4 fm (a typical nuclear radius) from the nucleon and, hence, recombine with the partons of neighboring nucleons. This will result in a net depletion of partons with wee-x values in the nucleons of nuclei relative to those of "free" nucleons of hydrogen or deuterium, and a corresponding enhancement of medium-x partons. This description accounts for both shadowing and antishadowing. The resultant behavior of this description is predicted to have very little dependence on the value of Q^2 of the interaction.

However, just a simple argument based on the uncertainty principle can suggest why this shadowing occurs at low $x_{\rm Bj}$ and low Q^2 [19]. This involves using the language of "old-fashioned perturbation theory" to discuss the dissociation of the photon into a virtual quark-antiquark pair. This quark-antiquark pair must separate by a distance, in the lab frame, of the size of a hadron (1 fm) before it can be "dressed" to interact like a hadron; this separation requires some minimum time, for example 1 fm/c. Consequently, this virtual state must commence far enough upstream of the target nucleon and survive long enough to reach it. In addition, this longitudinal extension must include the full length of the nucleus for the virtual state to probe the full volume and, therefore, experience the full amount of shadowing.

This distance depends upon the time which, according to the uncertainty principle, is inversely proportional to the energy difference ΔE of the state of the virtual photon and the state of the separating quark-antiquark pair,

which is of mass m in the pair's rest frame. This energy difference can be written as

$$\Delta E = \sqrt{\nu^2 - q^2 + m^2} - \nu \tag{15}$$

$$\approx \frac{Q^2 + m^2}{2\nu}, \tag{16}$$

for $\nu^2 \gg Q^2$. Thus, the longitudinal extension of the separating quark-antiquark pair can be written as

$$\Delta S_{\parallel} \approx c\Delta t \geq \frac{1}{x_{\rm Bj} M} \frac{Q^2}{Q^2 + m^2}. \tag{17}$$

Typical values of the mass m of the separating pair are on the order of $\sqrt{Q^2}$, so the transverse separation has a typical value:

$$\Delta S_{\perp} \approx 1/m \sim 1/\sqrt{Q^2}. \tag{18}$$

Then, for the transverse separation to be about 1 fm, Q^2 must be very small: $Q^2 < 0.04$ GeV$^2/c^2$. For the state to exist for many (10) fm of longitudinal extension, the $x_{\rm Bj}$ must also be small: $x_{\rm Bj} < 10^{-2}$. Empirically, the cross sections on nuclear targets exhibit a depletion at low $x_{\rm Bj}$ relative to a simple proton-neutron isoscalar target, but it persists to higher values of Q^2 [5,6].

E. Hadronization

The preceding discussion of shadowing involved only the comparisons of the total cross sections for the interactions, without knowledge of final state hadrons. E665 had the apparatus for good coverage of the final state hadrons as well. In hadron-nucleus collisions, where the cross sections exhibit shadowing, there has been observed a correlated attenuation of final state hadrons [7,20]. This attenuation can be described as the x_F (or z) dependence of the ratios of invariant cross sections of hadron-nuclear final state hadron production. In Ref. [21] these ratios of hadron distributions from the reactions $pA \to X$, at incident energies from 24 to 400 GeV, were fit to a form $A^{\alpha(x_F)}$, where the dependence of the exponent α on x_F was expressed in a simple polynomial form:

$$\alpha(x_F) = 0.74 - 0.55x_F + 0.26x_F^2; \tag{19}$$

the fit included a range of x_F of $\{0.1, 0.9\}$ at P_t of 0.3 GeV/c and had a reduced χ^2 of 0.7.

We wish to compare this final state hadron attenuation from hadron-nucleus collisions to the final state hadron differential distributions from our analysis of muon-nucleus collisions. Since we have normalized our distributions to the number of scatters, we must scale-out the values of the total cross sections for the hadron-nucleus data. The A dependence of the inelastic cross section of proton-nucleus scattering has been parametrized as $38.2A^{0.72}$ mb, for an incident energy of 100 GeV [22]. The form of Eq. (19) does not extrapolate correctly to hydrogen [21], but, for estimating the magnitude of the attenuation in a comparison of xenon over deuterium, we assume that deuterium can be treated as a comparable nucleus of $A = 2$. Thus, the ratio of the x_F dependence for the two targets, with the A dependence of the total cross section divided out, would follow the form

$$\text{ratio} = \left(\frac{A_{\rm Xe}}{A_{\rm D_2}}\right)^{\alpha(x_F) - 0.72}. \tag{20}$$

We plot this form in Fig. 2 as our hypothesis of how the attenuation would appear in the ratios of the normalized differential hadron distributions for xenon over deuterium, if the attenuation were equivalent to that seen in hadron-nucleus collisions. Clearly, there should be less production of high-x_F final state hadrons from nuclear targets than from a simple nucleon (hydrogen) target, and from the xenon target this would be very pronounced. Our analysis involves a search for such attenuation in deep-inelastic scattering in the shadowing region.

The process of hadronization has no basic theory but is usually described by phenomenological models. These models are all based on intuitive pictures of the evolution of the interaction into final state hadrons. The distributions of final state hadrons can be influenced by the effects of several processes. The relative times of commencement and durations of these processes will influence the final state of the system. Typically, the generation of hadrons in deep-inelastic scattering can be described in two stages. The first process is the creation of the intermediate "excited" state in the nucleon by the absorption of the virtual photon. The second process is the evolution of the excited state into final state particles — the process of fragmentation and hadronization. These processes can be investigated using the two distributions of Field and Feynman [23]: the *constituent functions* $q_i(x)$ [which they called $G_{h\to q}(x)$] and the *fragmentation functions* $D_q^h(z)$.

The constituent distributions $q_i(x)$ represent the distributions of constituents of the struck nucleon, carrying momentum fraction x; these were based on the SU(3) description of quarks and constructed from measurements

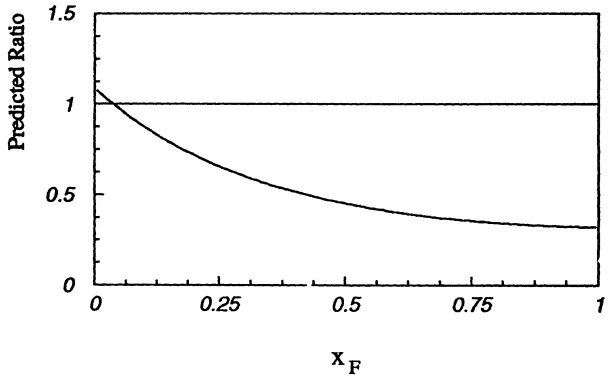

FIG. 2. Hadron-nuclear attenuation. Using Eq. (20), we predict how the attenuation should appear in the ratios of the normalized differential hadron distributions for xenon over deuterium.

of deep-inelastic structure functions. The fragmentation functions $D_q^h(z)$ represent the probability distributions of a constituent q disintegrating into a hadron h carrying momentum fraction z of that of the constituent. When examining both positively and negatively charged pions, one should be able to factorize the total hadron production cross section into the scattering cross section and the fragmentation function, where the latter does not depend on the event variables [23].

Qualitatively, the creation of the excited state should depend upon the constituent distributions and the event kinematics. The excited state propagates for some time before the formation of hadrons; this time is called the *constituent length* [24]. The interactions of the excited state with the rest of the nucleon and with the other nucleons in a nucleus occur during this time. At some point, this state fragments into hadrons, a process which is called *fragmentation.* The *formation length* is the time required for several partons to become a hadron [25,26]; this length is subject to Lorentz dilation and is often approximated by $\tau \geq E_h/m_h^2$. The formation time is taken as an extension of the Landau-Pomeranchuk phenomenon; the partons which form the hadron start out close together and screen each other from interacting strongly with the nucleus until after they separate enough [25]. For a pion of a few GeV, this formation completes after a distance of several fermi and, hence, outside of a nucleus. Thus, the interaction of the final state hadrons with the struck nucleus is expected to be a small effect and is ignored in this analysis.

Therefore, any observed effects of nuclear targets on the distributions of final state hadrons would be due primarily to interactions of the excited state traversing the rest of the nucleons of the nucleus. Then, the distributions of the final state hadrons from a nuclear target could be expressed as the sum of contributions from excited states which interacted and from those that fragmented unaltered [26]:

$$D_A(z) = (1 - I_{qN})D_N(z) + I_{qN} \int_z g(x|z)D_N(x)dx. \quad (21)$$

Here, $D_N(z)$ is the distribution of hadrons from a nucleon target, I_{qN} is the total probability of rescattering of the excited state, and the function $g(x|z)$ describes how the hadronic z distribution is modified by the rescattering of the excited state.

In this analysis we examine the final state hadron distributions as functions of the hadron energy fraction z. In the regime of shadowing, the picture of the virtual photon interacting as a hadron suggests that the final state hadrons should display characteristics of hadron-nuclear collisions, which should then depend upon the atomic weight of the target nucleus. Such differences would indicate that the propagation of the excited state is hadronlike. This should appear as an attenuation of the distribution of final state hadrons.

F. Measurements

We measured the incident muons in the beam spectrometer, analyzing the momentum in a dipole magnet. The scattered muons were tagged by their passage through 3 m of steel into the muon proportional chambers. We measured charged particles in the forward spectrometer, analyzing their momentum in a dipole magnet; the muon track in the muon spectrometer was matched to the appropriate track in the forward spectrometer. All of the event kinematics were calculated from the information from the incident and scattered muon tracks.

Electrons and photons were reconstructed in an electromagnetic calorimeter; tracks pointing to clusters in the calorimeter were removed from the "hadron" samples. No other particle identification was utilized in this analysis. The hadron sample comprised the rest of the tracks in the forward spectrometer. In calculating energies of particles, we assumed the mass of a pion for all hadron tracks.

The fiducial acceptance of the forward spectrometer was about 95% for particles with momentum greater than 20 GeV/c, and it fell off below this momentum. The efficiency of reconstruction was nearly flat at about 80%. We refer to the correction for these two effects as correction for *acceptance.* We discuss the details in Appendix A 6.

G. Event kinematics: $\mathbf{Kin_1}$ and $\mathbf{Kin_2}$

The effect of *shadowing* has been observed as a depletion of the scattering cross section in a "low" range

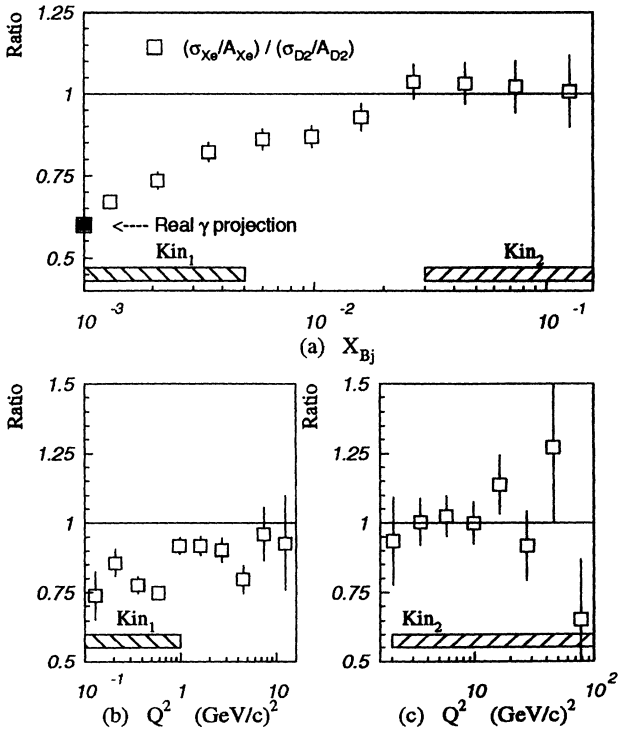

FIG. 3. Shadowing in cross section ratios. These plots show the effect of shadowing in the ratios of cross sections. In plot (a) the ratio is shown as a function of x_{Bj}. In plot (b) is shown the dependence of the ratio on Q^2, for a range of $0.001 < x_{Bj} < 0.025$. In plot (c) is shown the dependence of the ratio on Q^2, for $0.025 < x_{Bj} < 0.20$. The systematic uncertainty on these ratios is 6%. These data are tabulated in Table XIV.

of kinematics. In Fig. 3 we show the cross section ratios of xenon over deuterium; these data have been corrected for radiative processes and acceptance. The data in Figs. 3(a) and 3(b) have been presented previously [6]. Fig. 3(a) shows the cross section ratios for xenon over deuterium as a function of x_{Bj}; at the higher values of x_{Bj} the ratio is consistent with unity, but at the lower values there is a depletion. The black point is a projection to real photon scattering from xenon; the quoted value and uncertainty of the photoproduction point (0.60 ± 0.03) results from the propagation of the statistical errors of the data through the A-dependent and energy-dependent fits used to interpolate and extrapolate to a xenon target at a photon energy of 150 GeV [27]. This value is consistent with the simple ratio $A^{0.9}/A$, with $A_{\mathrm{Xe}} = 131$. Fig. 3(b) shows the cross section ratio as a function of Q^2 for the interval of $0.001 \leq x_{\mathrm{Bj}} \leq 0.025$, and Fig. 3(c) shows the cross section ratio as a function of Q^2 for the interval of $0.025 \leq x_{\mathrm{Bj}} \leq 0.20$.

To study the final state hadron distributions, we wish to isolate events from two kinematic regions Kin_1 and Kin_2, in one of which shadowing is apparent while in the other it is not. These two regions can be seen graphically in Fig. 3 as the hatched boxes. We define the "low kinematic range" (Kin_1) as the shadowing region:

$$\mathrm{Kin}_1 \equiv \begin{cases} x_{\mathrm{Bj}} < 0.005, \\ Q^2 < 1\ \mathrm{GeV}^2/c^2. \end{cases} \tag{22}$$

We also define a "high kinematic range" (Kin_2) as the nonshadowing region:

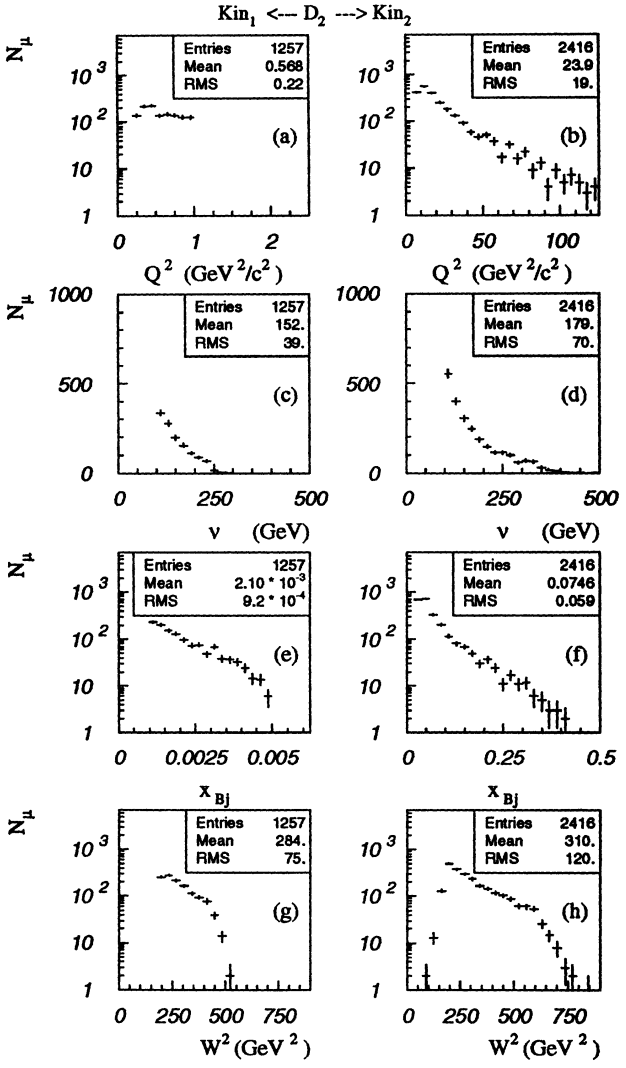

FIG. 4. Kinematics for Kin_1 and Kin_2, D_2. These plots indicate the distribution in event kinematics of the actual data samples used in the hadron analysis; they are, consequently, not corrected for any acceptance. The plots on the left are from the low kinematic region, Kin_1; the plots on the right are from the high kinematic region, Kin_2. These data are tabulated in Tables XV to XVIII.

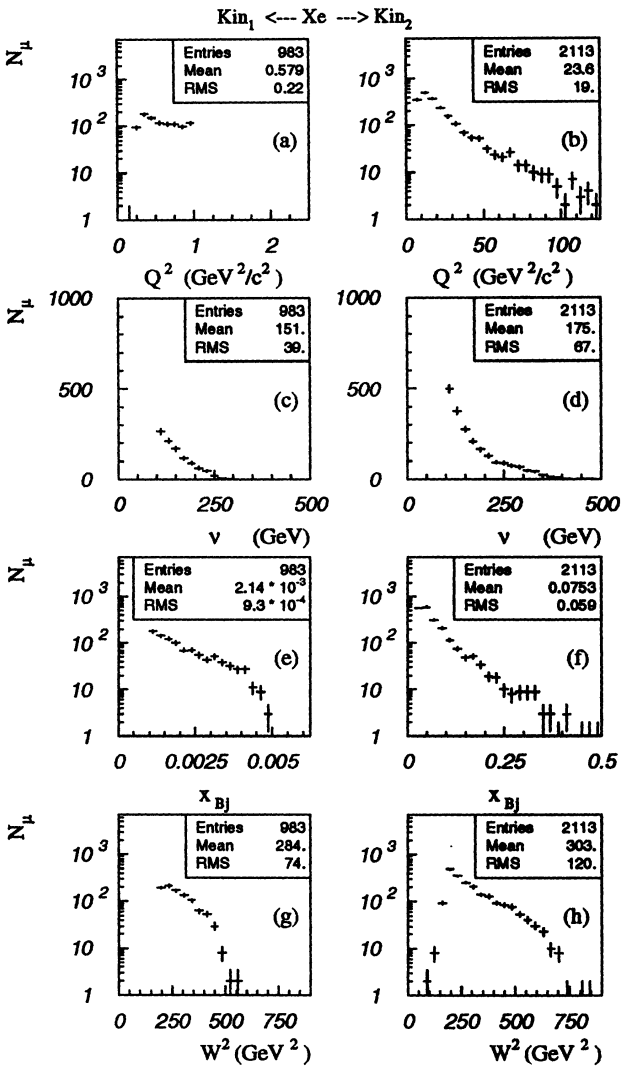

FIG. 5. Kinematics for Kin_1 and Kin_2, xenon. These plots indicate the distribution in event kinematics of the actual data samples used in the hadron analysis; they are, consequently, not corrected for any acceptance. The plots on the left are from the low kinematic region, Kin_1; the plots on the right are from the high kinematic region, Kin_2. These data are tabulated in Tables XV– XVIII.

$$\text{Kin}_2 \equiv \begin{cases} x_{\text{Bj}} > 0.03, \\ Q^2 > 2\ \text{GeV}^2/c^2. \end{cases} \quad (23)$$

The actual distributions of the events used in the hadron studies are shown as functions of the kinematic variables Q^2, ν, x_{Bj}, and W^2, for these two kinematic regions for deuterium in Fig. 4; the distributions for these two regions for the xenon samples are shown in Fig. 5. It can be seen from the statistics in the figures that these two samples, with intentionally disparate ranges of Q^2 and x_{Bj}, have similar distributions in ν and W^2. These data are tabulated in Appendix B.

The selection of the event samples involved elimination of backgrounds, using calorimetry as well as restrictions on the ranges of the event kinematic variables. For example, the lower limit on x_{Bj} for practical use in final state hadron studies was about $x_{\text{Bj}} = 0.001$, because of the overwhelming amount of electromagnetic background below this value. In our previous work on cross section ratios [27], lower values of x_{Bj} were analyzed, but the use of calorimetry for the removal of electromagnetic backgrounds was validated by hadron requirements, which we cannot use in this analysis. Elimination of background events was often facilitated by rejecting a range of a particular kinematic variable upon which the background events depended strongly. As the variables are interrelated, the cuts in one variable affected the ranges of other variables. Consequently, the final kinematic ranges of the event samples, shown in Figs. 4 and 5, result from a suite of cuts, which are detailed in Appendix A. (The two-dimensional plot of Q^2 versus y in Fig. 28 in Appendix A 5 helps to give an impression of the correlation of the kinematic variables.)

III. *Z* DISTRIBUTIONS

A. Comparison with previous data

In Fig. 6 are plotted the z distributions of charged hadrons from E665, as well as several previous experiments: EMC [3], and CHIO from several kinematic regions [4,28]. These data lie within the range of z of

$$\{z_{\text{min}},\ z_{\text{max}}\} = \{0.05,\ 0.95\}; \quad (24)$$

all of the data distributions in our analysis lie within this range.

The E665 data are from the sample of "high-kinematics" (Kin_2) scatters from the deuterium target. These data have been corrected for both acceptance and target length effects, which are discussed in detail in Sec. IV, and may be taken as *fully* corrected. They are consistent with those from previous experiments, which were from scatters from hydrogen targets. The data samples cover a large range of kinematics of the lepton scattering; the fact that the charged hadron distributions are so similar suggests that the factorization approximation is valid for these ranges of kinematics of the scattering.

The z distribution from this analysis is also consistent with that previously published by E665 [29]; the distributions were obtained from the same data sample, but with a slightly different set of kinematic restrictions and corrections. Of special interest is the fact that the previous z distributions were corrected for radiative processes using a Monte Carlo simulation of the electromagnetic contamination, while this analysis has used calorimetry to remove events due to electromagnetic interactions. The fact that the final distributions agree within experimental error lends credence to the two methods. The details of the calorimetry are discussed in Appendix A 5.

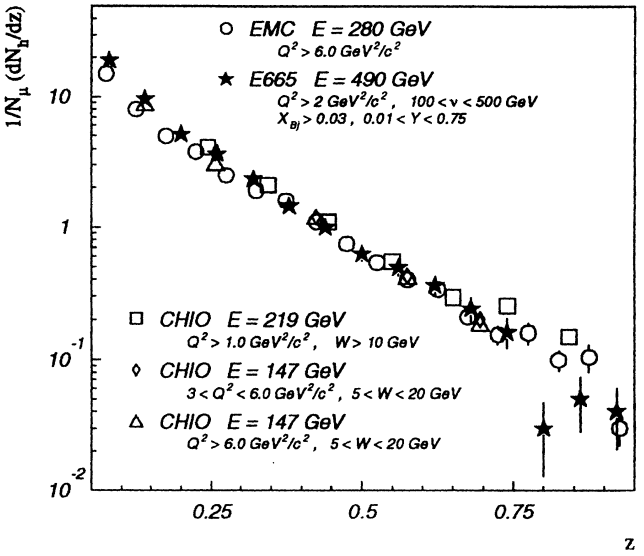

FIG. 6. Previous z distributions. These plots show the z distributions from E665 and from EMC [3], CHIO at 147 GeV [4], with CHIO at 219 GeV from Ref. [28]. The E665 data have been fully corrected and are the same as those presented later in Fig. 13(b).

B. Xenon versus deuterium

The objective of this analysis is to determine the influence of nuclear matter on the final states of the produced hadrons. The effect of *shadowing*, discussed in Sec. II D, has been observed as a depletion of the scattering cross section in a "low" range of kinematics, indicating a strong dependence of the scattering cross section on the number of nucleons in the target. However, no such strong nuclear dependence appears in the distributions of produced hadrons from this kinematic region.

The z distributions from the xenon and deuterium targets are compared in Fig. 7, for both kinematic regions, low and high. The plots on the left contain the z distributions for Kin_1, the "low" range of kinematics; those on the right contain the z distributions for Kin_2, the "high" range of kinematics. The distributions from the xenon target are at the top of each column, while those from the deuterium target are second; the ratios of the distributions, Xe/D_2, are plotted at the bottom of each column. These data have been corrected only for acceptance and not for target length effects, which we discuss in Sec. IV.

The z distributions were fit in the central region, $z \in \{0.23, 0.83\}$, to an exponential form:

$$D(z) = \exp[\text{const} + \text{slope}\ z], \tag{25}$$

and the values of the parameters are included on the plots. The reduced χ^2's (χ^2 per degree of freedom) from the fits are shown on the plots as $\chi^2/N_{\rm DF}$. This model for a fit is simplistic, since it must fail at very low z, where the distributions diverge like $1/z$ [23(b)], and also at high z, where the distributions must vanish due to the kinematic limit. Nevertheless, in the central-z region, the model fits reasonably well. We should note that since the distributions are basically exponential, the fit is heavily weighted by the lowest couple of points included in the fit, and hence the parameters of the fit depend heavily upon the choice of the minimum value of z included in the fit.

There are several ways of comparing the distributions to ascertain whether they could belong to different parent distributions. The simplest is to follow the model of the exponential parent distribution and to compare the parameters of the fits of the corresponding data distributions along with the errors on those parameters. The parameters of the data distributions from both targets and both kinematic ranges are all within one σ of each other.

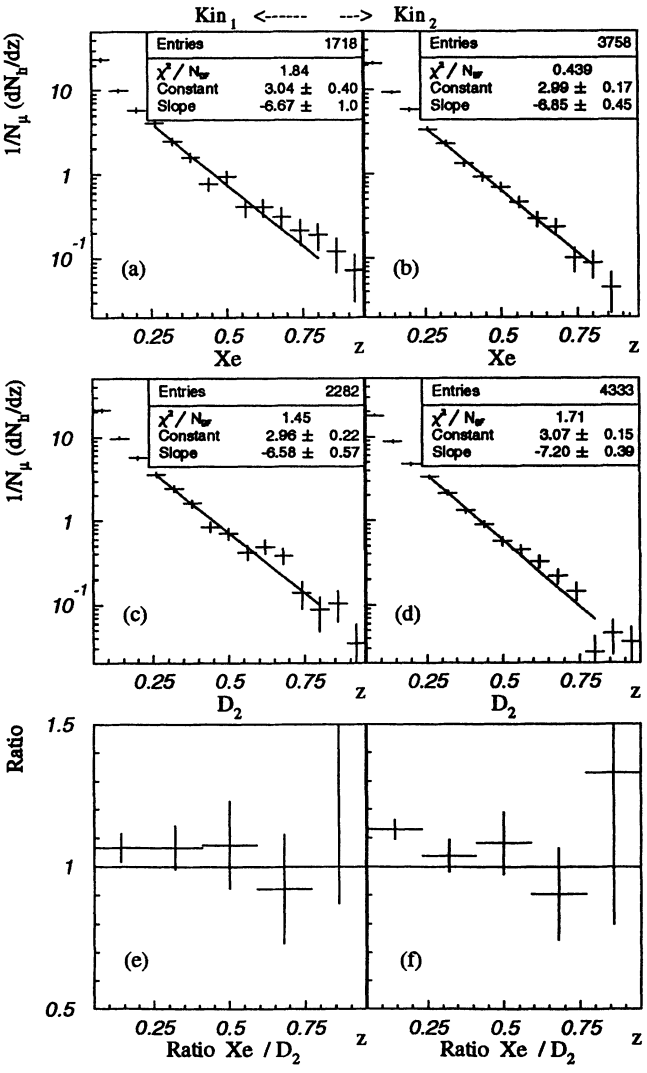

FIG. 7. z distributions: Xe and D_2. These plots show the z distributions from xenon and deuterium and the ratios of the distributions. The distributions on the left are from events in the low kinematic region: Kin_1, while those on the right are from events in the high kinematic region: Kin_2. The data have been corrected for acceptance but not for target length effects; they are tabulated in Tables XIX and XXX.

The next simplest comparison is to take the ratios of the data distributions. These are plotted in Figs. 7(e) and 7(f). The ratios indicate that these distributions are consistent between the two targets, for both regions of kinematics. In fact, the distributions are consistent for the two kinematic regions for a single target. In Fig. 8 we have plotted the ratios of the z distributions for the low-kinematic region over the high-kinematic region; the ratio for the xenon target is plotted in Fig. 8(a), and the ratio for the deuterium target is plotted in Fig. 8(b). These ratios are both consistent with unity, within our statistical and systematic error of 14%. This indicates that the hadron distributions are not dependent strongly upon the kinematics of the initial scattering and justifies considering the factorization approximation, even across these disparate kinematic ranges; we only needed it to hold within each kinematic range separately.

More sophisticated approaches can yield more precise exclusions of parent distribution similarity. One common approach is to integrate over a range of z, yielding a partial multiplicity, and to take the ratio of these quantities. We define this integration $R_{\rm sample}$ as

$$R_{\rm sample} \equiv \frac{\sum_{Z_{\rm min}}^{Z_{\rm max}} D_{\rm sample}(z_i)\ \Delta z}{Z_{\rm max} - Z_{\rm min}} \tag{26}$$

and the error $\sigma_{R_{\rm sample}}$ as

$$\sigma_{R_{\rm sample}} \equiv \frac{\Delta z}{Z_{\rm max} - Z_{\rm min}} \sqrt{\sum_{Z_{\rm min}}^{Z_{\rm max}} \sigma^2_{\rm D_{sample}(z_i)}}. \tag{27}$$

The ratio can be expressed as the function $\overline{R}_A$:

$$\overline{R}_A \equiv \frac{R_A}{R_{\rm D_2}}; \tag{28}$$

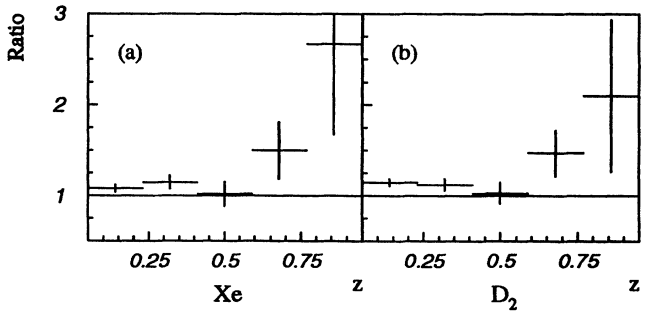

FIG. 8. Ratio of kinematic regions. These plots show the ratios of the z distributions for the low kinematic region over the high kinematic region, for the xenon target in (a) and for the deuterium target in (b). The data from these plots are tabulated in Table XXXI.

the error on the quantity is given by $\sigma_{\overline{R}_A}$:

$$\sigma_{\overline{R}_A} \equiv \overline{R}_A \sqrt{\frac{\sigma^2_{\overline{R}_A}}{R^2_A} + \frac{\sigma^2_{\overline{R}_{D_2}}}{R^2_{D_2}}}. \quad (29)$$

To be consistent with the range used in the fit of Eq. (25), we have used the following limits of integration for these comparisons:

$$\{Z_{\min},\ Z_{\max}\} = \{0.23,\ 0.83\}. \quad (30)$$

The values of $\overline{R}_A$ from the comparisons of the data distributions are listed in Table I. The comparisons of xenon to deuterium are within 1σ of unity.

Because of the steeply falling nature of the z-distributions, the lowest-z points dominate the values of the sums, and the value of the ratio could depend on the choice of $Z_{\min}$. If the distributions were of different slopes but were to cross at a z just above the choice of $Z_{\min}$, then the value of $\overline{R}_A$ would still be close to unity. So, this method, although common, has some weakness in distinguishing certain distributions.

Another approach which is more sensitive to differences in the high-z end of the distributions is to calculate a reduced-χ^2 difference of the two data distributions. This can be expressed as a normalized weighted difference of the two distributions:

$$\chi^2_A \equiv D_A(z) \ominus D_{D_2}(z) \equiv \frac{1}{N_{DF}} \sum_{Z_{\min}}^{Z_{\max}} \frac{[D_A(z) - D_{D_2}(z)]^2}{\sigma^2_{D_A(z)} + \sigma^2_{D_2(z)}}. \quad (31)$$

The range of the summation is given, again, by Eq. (30), and the number of degrees of freedom was 10. The probability that the two samples came from the same parent distribution is given by $P_{\chi^2_A}$. The values of χ^2_A and $P_{\chi^2_A}$ from the comparisons of the data distributions are listed in Table II. If the compared distributions came from the same parent distribution, then the values of $P_{\chi^2_A}$ should be distributed between 0 and 1 with equal probability. Only for small values of $P_{\chi^2_A}$ can we exclude the hypothesis that the two samples originated from the same parent distribution; we require that $P_{\chi^2_A} < 0.05$, yielding a confidence level of 95%. For probabilities greater than this, we cannot differentiate between the samples. From the $P_{\chi^2_A}$ numbers in Table II, we cannot exclude similarity of the xenon and deuterium z distributions for either kinematic range at the 95% confidence level.

We can also use these functions to compare the distributions from the two kinematic ranges for each target. The definitions of $\overline{R}_A$ and χ^2_A can be generalized, using the distributions from Kin_1 as the numerator and those from Kin_2 as the denominator for these calculations. The values of $\overline{R}_A$ from these comparisons of the data distributions are listed in Table I, and the values of χ^2_A from the comparisons of the data distributions are listed in Table II. From the numbers in Table II, we cannot exclude similarity of any of the distributions at the 95% confidence level.

TABLE I. $\overline{R}_A$ values. These values are from the comparison function of Eq. (28) for the listed comparisons.

	$\overline{R}_A$	±	$\sigma_{\overline{R}_A}$
Xe / D_2 (Kin_1)	1.06	±	0.07
Xe / D_2 (Kin_2)	1.04	±	0.05
Kin_1 / Kin_2 (D_2)	1.14	±	0.06
Kin_1 / Kin_2 (Xe)	1.16	±	0.07

TABLE II. χ^2_A values. These values are from the comparison function of Eq. (31), for the listed comparisons. The number of degrees of freedom was 10.

	χ^2_A	$P_{\chi^2_A}$
Xe ⊖ D_2 (Kin_1)	0.67	0.75
Xe ⊖ D_2 (Kin_2)	0.62	0.80
Kin_1 ⊖ Kin_2 (D_2)	1.32	0.22
Kin_1 ⊖ Kin_2 (Xe)	1.32	0.21

IV. RESCATTERING IN TARGET

A. Target length effects

Hadrons produced in the initial scattering event must traverse the rest of the target material before entering the spectrometer, and there is some probability that they will interact with this material. Since the deuterium target was nearly a third of an interaction length long (see Table VIII), we have examined the effects of this rescattering. The rescattering in the target material would tend to "soften" (i.e., steepen) the observed hadron distributions, and it might also effect a net loss of tracks assigned to the primary vertex. Thus, the effect of final state hadron rescattering in the deuterium target could produce steepening similar to that from nuclear attenuation of the interaction in the xenon nucleus, and therefore prevent us from measuring the nuclear effect in our comparisons.

To study the effects of rescattering in the targets, we have examined the hadron distributions separately from three successive segments of the targets, from upstream to downstream. We have included all the data from the full kinematic range. The normalized z distributions from each third of the target have been corrected for detector acceptance independently. We compare the distribution from the most upstream third of the deuterium target, in which rescattering should have the most pronounced effect, to that from the downstream third. The distributions from these two regions are overlaid in Fig. 9(a), in which the distribution from the upstream segment is represented by the circles, connected by a solid line, while that from the downstream segment is represented by the triangles, connected by a dashed line. The points have been connected by different line types merely to aid the eye. The difference is not very large on a log plot; consequently, we present the ratios of the most upstream regions over the most downstream regions for

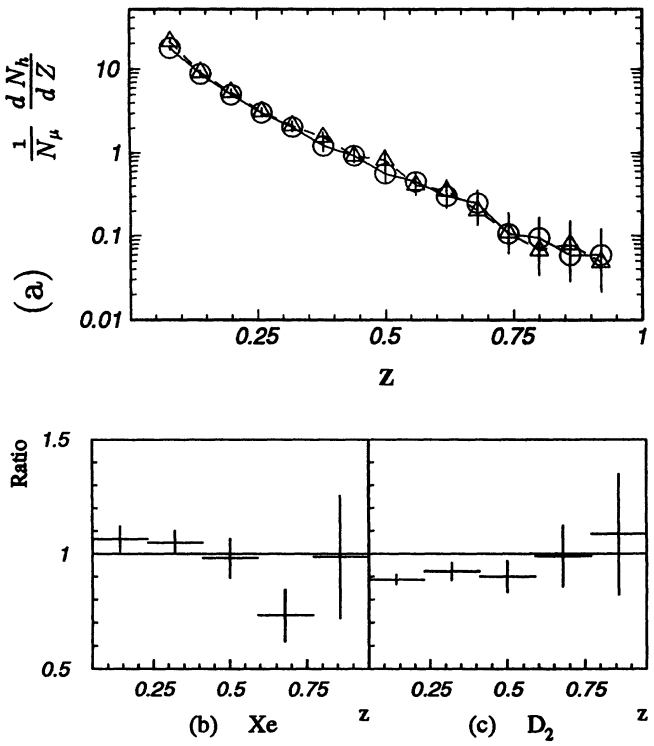

FIG. 9. Comparison of upstream and downstream segments of targets. In (a) the circles represent the distribution from the upstream third of the D_2 target, while the triangles represent that from the downstream third. The ratios of the upstream over downstream distributions are shown in (b) for the xenon target and in (c) for the deuterium target.

the two targets: the ratio for the xenon target is shown in Fig. 9(b), while that for the deuterium target is shown in Fig. 9(c).

There is little evidence of target length effects in the xenon sample, in which the ratio of the distributions from the upstream and the downstream segments look consistent with unity. The corresponding value of the $\overline{R}_A$ function for the comparison of the upstream and downstream segments of the xenon target is 1.008 ± 0.041, and the corresponding $P_{\chi^2_A}$ value is 0.146. These values may be found in Tables III and IV, respectively.

On the other hand, it is clear that more low-z tracks were lost in the upstream end of the deuterium target than in the downstream end, with a depletion of the ratio from unity by about 10%. The value of the $\overline{R}_A$ function is 0.925 ± 0.033, and the $P_{\chi^2_A}$ value for the comparison is 0.056, which is significantly low at the 90%

TABLE III. Target length $\overline{R}_A$ values. These values are from the comparison function of Eq. (28) for the listed target length comparisons.

	$\overline{R}_A$	$\pm$	$\sigma_{\overline{R}_A}$
up / down (D_2)	0.925	$\pm$	0.033
up / down (Xe)	1.008	$\pm$	0.041
up / down (corrected D_2)	1.055	$\pm$	0.038
up / down (corrected Xe)	1.034	$\pm$	0.042

TABLE IV. Target length χ^2_A values. These values are from the comparison function of Eq. (31) for the listed target length comparisons. The number of degrees of freedom was 10.

	χ^2_A	$P_{\chi^2_A}$
up $\ominus$ down (D_2)	1.79	0.056
up $\ominus$ down (Xe)	1.46	0.146
up $\ominus$ down (corrected D_2)	1.52	0.123
up $\ominus$ down (corrected Xe)	1.52	0.124

confidence level. These values also may be found in Tables III and IV, respectively. For the lowest bin in z in the ratio plots, the acceptance corrections were quite large ($\sim 50\%$), so the systematic uncertainty on that bin is 20%; we have excluded this first point in the comparisons.

From the ratios in Figs. 9(b) and 9(c), we conclude that there is little evidence of target length effects in the xenon, but a clear indication of rescattering in the deuterium target. We attempt to remove this target position dependence in the next section.

B. Deconvolution

1. Method

The removal of target length effects can be expressed as a deconvolution of the measured distribution of hadrons in the final state, $D_f(z)$, back into an ideal distribution of hadrons produced in the initial scattering, $D_i(z)$. The modification of the initial distribution by any rescattering that occurs can be expressed as a Fredholm equation [30]:

$$D_f(z) = \int_{-\infty}^{\infty} K(x|z)\ D_i(x)dx, \tag{32}$$

where the function K, the *kernel*, describes the convolution of the initial distribution into the final distribution. In this particular case, for a hadron which rescatters inelastically, the final fraction of energy carried away, z, will be less than that which it initially possessed, x. For hadrons which do not rescatter, the energy carried away will remain unchanged: $z = x$. Consequently, the kernel can be written as two terms:

$$K(x|z) = (1 - I)\ \delta(x - z) + I\ H(x|z), \tag{33}$$

where the value I is the probability of rescattering. The rescattering function, $H(x|z)$, is defined on the interval of $x : 0 \leq z \leq x \leq 1$; it shuffles the population of hadrons of scaled energies x to lower values z within this interval. We use a constant rescattering probability since the inelastic π-D_2 cross section is roughly independent of energy for pions above 10 GeV. It is also small enough that we ignore plural scattering.

Thus, the modified distribution of final states, $D_f(z)$, can be expressed as the sum of two terms; the first term is due to the unrescattered hadrons, and the second term is due to the hadrons which rescattered in the rest of the

target material:

$$D_f(z) = (1 - I)\ D_i(z) + I\ G(z). \tag{34}$$

This second term $G(z)$ is a convolution of the original ideal distribution $D_i(z)$ with a rescattering function $H(x|z)$:

$$G(z) = \int_{-\infty}^{\infty} H(x|z)\ D_i(x)dx. \tag{35}$$

Equation (34) is analogous to Eq. (21) of Sec. II E.

There are several mechanisms by which the rescattering in the target can effect a net loss of tracks assigned to the primary vertex. One loss is the production of neutral particles from the secondary scattering, which would be missed since only charged particles were studied. Another loss is due to the reconstruction of vertices; tracks from rescattered hadrons may not be assigned to the primary vertex since they will appear "kinked" at the rescattering point. Since this analysis examines only tracks assigned to the primary vertex, those tracks which were lost from the vertex assignment will be lost from the sample.

We attempt to account for these rescattering losses with an efficiency function ϵ in the convolution, as a factor of the rescattering function $H(x|z)$. In principle, this function could depend upon the hadron's energy fraction as well as the positions in the target of the initial and secondary scatters. In practice, it has been possible to average over these dependences and to use a simple constant value for ϵ; this value has been chosen by examination of a Monte Carlo study of rescattering. Fully reconstructed tracks from rescatters were tested for assignment to the primary vertex; the efficiency for this assignment is plotted in Fig. 10. The sample studied included only tracks truly from secondary scatters, according to the Monte Carlo simulation; this sample was further restricted to contain only those tracks which were reconstructed in the forward spectrometer. Then the determination of efficiency of assignment to the primary vertex was made. The z dependence of this function was based on the true value of z of the hadron after rescattering; no smearing due to reconstruction was considered.

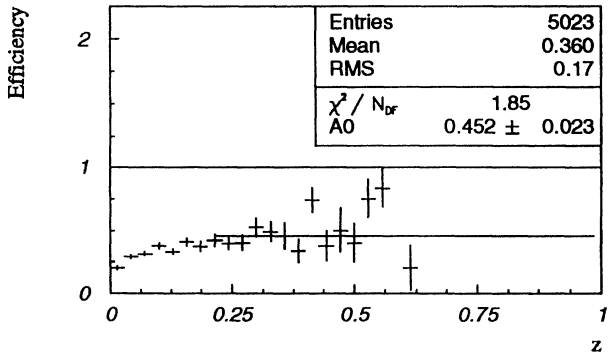

FIG. 10. Rescattering loss parameter. This plot shows the *efficiency* of linking rescattered tracks to the primary vertex, as a function of the tracks value of z. This is based on a Monte Carlo study.

2. *Probability of rescattering*

The probability of rescattering, I, can be expressed as a function of the fraction of pion-interaction lengths of material traversed by the hadrons before exiting the target. We take L_π to represent the length of the target in terms of the π-D_2 inelastic interaction length and $\{t_1, t_2\}$ to represent an arbitrary segment of the target, in terms of the fractions of the target which are downstream of the segment. Then, with the assumption of a uniform distribution of initial scatters, the averaged rescattering probability for this segment is given by the equation [31]

$$I = 1 - \frac{\exp[-t_1 L_\pi] - \exp[-t_2 L_\pi]}{(t_2 - t_1)L_\pi}. \tag{36}$$

We restricted our event sample to lie *inside* the walls of the targets, so the thirds of the targets are described as follows. For the upstream third of the target, the fractions remaining to traverse are $\{t_1, t_2\} = \{1, 0.684\}$, and for the downstream third of the target, the fractions remaining to traverse are $\{t_1, t_2\} = \{0.368, 0.052\}$; for the full target length, the fractions remaining to traverse are $\{t_1, t_2\} = \{1, 0.052\}$. Using the value of $L_\pi = 0.225$ (from Table VIII), the average rescattering probabilities for the deuterium target are

$$I_{\text{up}} = 0.17,$$
$$I_{\text{down}} = 0.046,$$
$$I_{\text{D}_2} = 0.11.$$

Using the value of $L_\pi = 0.044$ from Table VIII, the average rescattering probabilities for the xenon target are

$$I_{\text{up}} = 0.036,$$
$$I_{\text{down}} = 0.010,$$
$$I_{\text{Xe}} = 0.023.$$

3. *Deconvolution of the target length*

The inverse operation involves deconvoluting a final distribution back to an ideal distribution. We have followed the treatment of Ref. [31]. The equation for the deconvoluted distribution, $D_m(z)$, can be written as

$$D_m(z) = \frac{1}{(1 - I)}\left[D_f(z) - I\ G_m(z)\right], \tag{37}$$

where $G_m(z)$ is the distribution of rescattering, calculated from the measured distribution and a chosen rescattering function $H(x|z)$. The rescattering function was chosen according to Ref. [31]; it incorporates the rescattering loss function ϵ.

The size of the unfolding can be seen in Fig. 11, in which the upstream segment of the deuterium target has been deconvoluted and overlaid on the measured distribution; also shown is the calculated rescattered distribution $G_m(z)$.

The deconvoluted distributions from both the up-

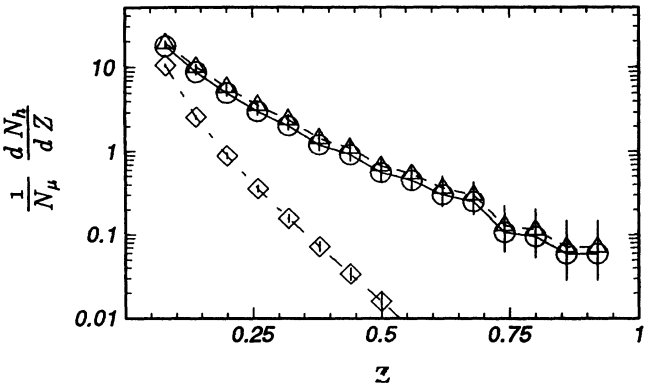

FIG. 11. Deconvoluted upstream segment of D_2 target. The circles represent the measured distribution from the upstream third of the target; the triangles represent the distribution deconvoluted from this measured distribution. The diamonds represent the calculated rescattered distribution.

stream and downstream segments of the deuterium target are recompared in Fig. 12(a), in which the distribution from the upstream segment is represented by the circles and the solid line while that from the downstream segment is represented by the triangles and the dashed line. The ratio of these deconvoluted distributions from the upstream and downstream segments of the deuterium target is shown in Fig. 12(c); it is much closer to unity across the z range than that in Fig. 9(c). The value of the $\overline{R}_A$ function for the comparison of the upstream and downstream segments of the deuterium target which have been corrected for rescattering is 1.055 ± 0.038; the $P_{\chi^2_A}$ value for this comparison is now 0.123, a significant improvement in similarity over 0.056; a 90% confidence level test no longer indicates a difference.

The equivalent ratio for the xenon target is shown in Fig. 12(b). The value of the $\overline{R}_A$ function for the comparison of the corrected upstream and downstream segments of the xenon target is 1.034 ± 0.042, and the corresponding $P_{\chi^2_A}$ value is 0.124. These values, of course, have not changed much from those from the uncorrected distributions since there was very little material from which to rescatter in the xenon target.

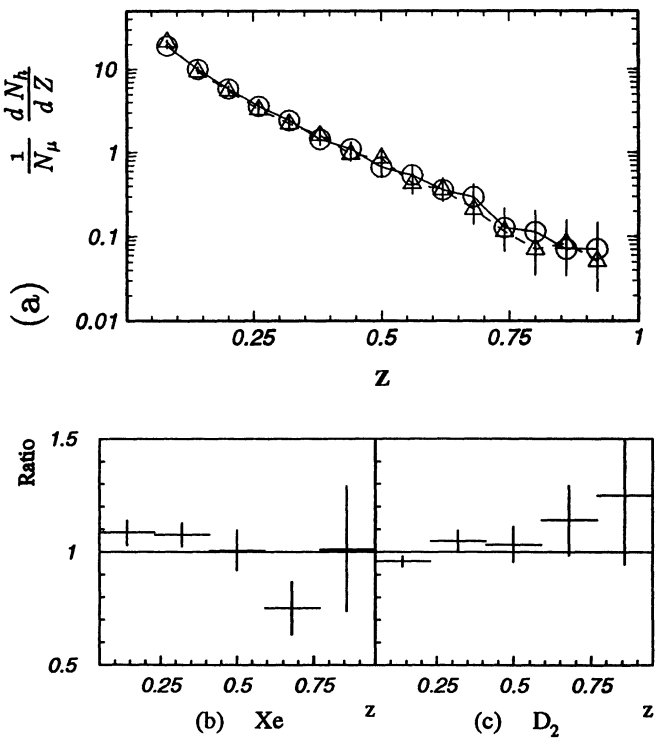

FIG. 12. Comparison of corrected upstream and downstream segments of targets. In (a) the circles represent the corrected distribution from the upstream third of the D_2 target, while the triangles represent that from the downstream third. The ratios of the upstream over downstream corrected distributions are shown in (b) for the xenon target and in (c) for the deuterium target. These plots may be compared to those in Fig. 9.

C. Corrected xenon and D_2

We now recompare the distributions from xenon to those from the deuterium target, both corrected for the target length effects. In Fig. 13(a) are shown the distributions from the low kinematic range Kin_1; those from the high kinematic range, Kin_2, are shown in Fig. 13(b). The distributions from the corrected deuterium are rep-

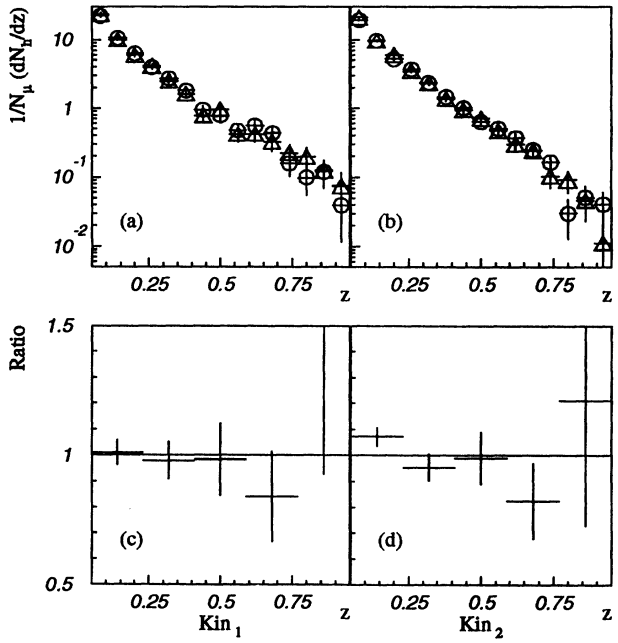

FIG. 13. Xe and D_2, corrected for rescattering. Plots (a) and (b) show the z distributions which have been corrected for rescattering in the targets. The circles represent the corrected deuterium distributions, while the triangles represent the corrected xenon distributions. The plots on the left are for the low kinematic region: Kin_1, while those on the right are for the high kinematic region: Kin_2. The ratio of these distributions is shown in (c) for Kin_1, and in (d) for Kin_2. These data are tabulated in Tables XX and XXXII.

TABLE V. Corrected $\overline{R}_A$ values. These values are from the comparison function of Eq. (28) for the listed comparisons; the comparisons used the distributions which were corrected for target length effects, except for the half-target samples.

	$\overline{R}_A$	±	$\sigma_{\overline{R}_A}$
Xe/D_2, (corrected Kin_1)	0.975	±	0.060
Xe/D_2, (corrected Kin_2)	0.957	±	0.044
Kin_1 / Kin_2 (corrected D_2)	1.134	±	0.058
Kin_1 / Kin_2 (corrected Xe)	1.156	±	0.066
Xe/D_2, (half) Kin_1	1.052	±	0.090
Xe/D_2, (half) Kin_2	0.990	±	0.064

resented by the circles while those from corrected xenon are represented by the triangles. The $\overline{R}_A$ values for these comparisons are listed in Table V, while the $P_{\chi^2_A}$ values for these comparisons are included in Table VI.

Also in Fig. 13 we have replotted the ratios of the corrected z distributions for the xenon and the deuterium. The ratios for the low-kinematic region are shown on the left in Fig. 13(c) and for the high-kinematic region on the right in Fig. 13(d). These ratios may be compared to those in Fig. 7, which did not include corrections for rescattering in the targets. The corrected ratios are lower but still consistent with unity. We conclude that the rescattering of the final state hadrons in the rest of the target material is not limiting our measurement.

Testing the validity of the deconvolution, we have examined the ratios of the z distributions for xenon over deuterium, restricting the samples to events in which the interactions occurred in the downstream *halves* of the targets. These data are tabulated in Table XXXIII and appear in Appendix B. No corrections for target length effects have been applied to these distributions. These ratios are consistent with unity; the $\overline{R}_A$ values for these comparisons are included in Table V, and the $P_{\chi^2_A}$ values are listed in Table VI. The statistics are lower than the full-target-length comparisons, and we cannot discern the reduced probability of rescattering in only half of the target material.

In Fig. 14 we have replotted the ratios of the z distributions for the low-kinematic region over the high-kinematic region, using the distributions which were corrected for target length effects. The ratio for the xenon target is plotted in Fig. 14(a), while that for the deuterium target is plotted in Fig. 14(b). The target length corrections divide out in these ratios. The ratios are both consistent with unity and indicate that the z distributions do not depend strongly upon the event kinematics of the initial scattering; they may be compared to those in Fig. 8.

TABLE VI. Corrected χ^2_A values. These values are from the comparison function of Eq. (31), for the listed comparisons; the comparisons used the distributions which were corrected for target length effects, except for the half-target samples. The number of degrees of freedom was 10.

	χ^2_A	$P_{\chi^2_A}$
Xe ⊖ D_2 (corrected Kin_1)	0.61	0.81
Xe ⊖ D_2 (corrected Kin_2)	0.64	0.78
Kin_1 ⊖ Kin_2 (corrected D_2)	1.30	0.22
Kin_1 ⊖ Kin_2 (corrected Xe)	1.32	0.22
Xe ⊖ D_2 (half) Kin_1	0.76	0.66
Xe ⊖ D_2 (half) Kin_2	0.67	0.76

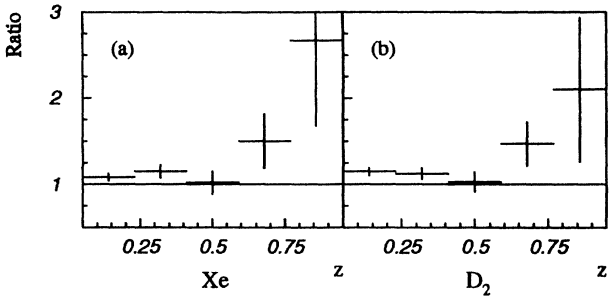

FIG. 14. Ratio of kinematic regions, corrected for rescattering. These plots show the ratios of the z distributions for the low kinematic region over the high kinematic region, for the xenon target in (a) and for the deuterium target in (b). These distributions have been corrected for rescattering in the targets. These data are tabulated in Table XXXIV.

We conclude that the z distributions from the xenon and deuterium targets, for both kinematic ranges, are consistent within errors. In the next section we estimate limits on the attenuation of the excited state in nuclear material.

V. RESCATTERING OF THE EXCITED STATE

As discussed in Sec. II E, a rescattering of the excited state in the rest of the nucleus would modify the distribution of the final state hadrons. This would appear as a steepening of the z distributions in xenon relative to deuterium, in the shadowing region Kin_1, if the initial interaction were hadronlike. In Fig. 13(a) the distribution from xenon is overlaid on the deuterium distribution, both of which have been corrected for target thickness. Since no such steepening of the xenon distributions is apparent, the level of rescattering of the excited state must be small. In order to quantify the limit of rescattering, we have examined the level at which the data can resolve a postulated effect.

Suppose that the excited state were like a hadron, similar to the picture of vector dominance. The initial interaction would occur near the surface of the nucleus, and this hadronlike state would propagate through the rest of the nuclear volume. The probability of this state reinteracting with the rest of the nucleus can be expressed as a function of the distance traveled in the nuclear material, d, the nuclear density n, and the cross section for the interaction of this exited state and nuclear material:

$$I = 1 - e^{-dn\sigma}. \tag{38}$$

Correspondingly, the cross section can be extracted from a measured interaction rate:

$$\sigma = -\ln[1 - I]/(n\ d). \quad (39)$$

For a hadron such as the pion, the inelastic cross section is $\sigma_{hN} \approx 20$ mb, and the collision length is given by $\lambda = [n\ \sigma_{hN}]^{-1}$. In heavy nuclei the nuclear density has the value $n = 0.170$ nucleons fm^{-3} [32(b)]. This gives a collision length of $\lambda = 2.9$ fm. A simple estimate of a nuclear radius, based on the model of an equivalent uniform-density sphere, is $R = r_0 A^{1/3}$, where $r_0 = 1.2$ [32(c)]. Thus, for xenon, with $A = 131$, the radius is $R_{\rm Xe} = 6.1$ fm. We have taken the radius of the xenon nucleus for a conservative estimate of the distance the excited state would travel through the nuclei: $d = R_{\rm Xe}$. Then, the probability of this hadronlike excited state interacting in the xenon nucleus would be given by Eq. (38) and would have a value $I = 0.87$.

The modified distribution of final states would be expressed by Eq. (21). The first term would be due to the hadronization of those excited states which did not rescatter in the nucleus, while the second term would be due to the hadronization of those which did rescatter. This second term is a convolution of the distribution of hadronization with that of the rescattering.

Using Eq. (21) and the formalism of Ref. [31], we have convoluted the measured xenon distribution to predict the appearance of the hadron distribution if the propagation of the excited state were hadronlike, and experienced nuclear rescattering. This is shown in Fig. 15 overlaid on the deuterium distribution which has been corrected for target length effects. Such a hadron-nuclear effect would have been visible easily with our statistical precision.

To achieve, for example, a 3σ effect in the $\overline{R}_A$ value in a comparison of the corrected deuterium and the convolution by nuclear rescattering of xenon would require a fraction of rescattering of $I = 0.125$; such a distribution is shown in Fig. 15 as the dashed line. From this upper limit on the fraction of rescattering and the distance of a radius of an equivalent spherical nucleus, we estimate from Eq. (39) that the data from the xenon and deuterium targets, in the region $\rm Kin_1$, could resolve a rescattering cross section, at the 3σ level, of 1.3 mb. The corresponding values of the $\overline{R}_A$ are included in Table VII.

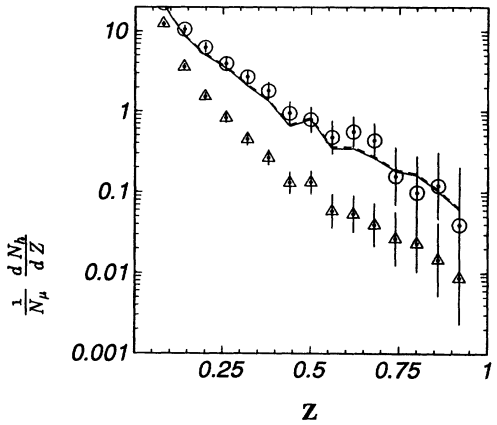

FIG. 15. $\rm Kin_1$, predicted Xe. This plot shows the corrected deuterium distribution for $\rm Kin_1$ as the circles. The triangles represent the predicted distribution for xenon if there were nuclear rescattering of the excited state. This distribution was convoluted from the measured xenon distribution for $\rm Kin_1$ to examine the statistical power of the comparison. The solid line represents the predicted distribution for xenon for which we could exclude similarity to the 95% confidence level, based on the χ^2_A test. The dashed line represents the predicted distribution for xenon which would yield a 3σ effect in $\overline{R}_A$.

TABLE VII. Rescattering limits, $\overline{R}_A$ values. These values are from the comparison function of Eq. (28) for the listed comparisons, using the distributions which were corrected for target length effects. The D_A/D_2 calculations were based on hypothesized attenuations.

	$\overline{R}_A$	$\pm$	$\sigma_{\overline{R}_A}$
D_A/D_2, nuclear, $\rm Kin_1$	0.168	$\pm$	0.009
D_A/D_2, nuclear, $\rm Kin_2$	0.156	$\pm$	0.006
D_A/D_2, 3σ, $\rm Kin_1$	0.843	$\pm$	0.052
D_A/D_2, 3σ, $\rm Kin_2$	0.878	$\pm$	0.040

To achieve an exclusion of similarity to the 95% confidence level using the χ^2_A comparison of the corrected deuterium and the convolution by nuclear rescattering of xenon would require a fraction of rescattering of $I = 0.164$. Such a distribution is shown in Fig. 15 as the solid line. From this upper limit on the fraction of rescattering and the distance of a radius of an equivalent spherical nucleus, we estimate that the data from xenon and deuterium targets, in the region $\rm Kin_1$, can exclude a rescattering cross section, at the 95% C.L., above 1.7 mb.

We conclude that the distributions of final state hadrons do not depend strongly on the target material or the kinematics of the event. Therefore, the production of final state hadrons in muon-nucleus scattering is different than in hadron-nucleus scattering which is summarized by Fig. 2.

VI. Z ORDERING OF FRAGMENTATION

A. Xenon versus deuterium, 1-2-3

In the fragmentation of the excited state into the final state hadrons, the available energy is divided among the final products. By examining the single-particle fractional energy distributions, we can gain some insight into the mechanism of energy distribution in fragmentation. In particular, we can investigate the similarity between these single-particle distributions in different regions of the kinematics of the initial scattering and in different nuclei.

To investigate these effects, we have examined the z distributions, using information regarding the *ordering* of the particles in terms of their energy. The particle with the highest z was referenced as the *fastest* particle. Similarly, the next highest-z particle was called the *second fastest*, and the third highest-z particle was called the *third fastest*. This involved only charged particles, so there was some "shuffling-up" of charged particles in the orders, as their preceding neutral sisters were missed. Also, inefficiencies in detection and reconstruction con-

tribute to this "shuffling" up the orders. In addition, in examining these single-particle distributions, we have ignored the effects of rescattering in the target, since it is a small effect and our statistical precision is less for these distributions.

The z distributions of the fastest particle from the xenon and deuterium targets are compared in Fig. 16, for both kinematic regions, low and high. The plots on the left include the z distributions for Kin_1, the "low" range of kinematics; those on the right include the z distributions for Kin_2, the "high" range of kinematics. The distributions from the xenon target are at the top of each column, while those from the deuterium target are second; the ratios of the distributions, Xe/D_2, are plotted at the bottom of each column. The ratios indicate that these distributions are consistent between the two targets, for both regions of kinematics.

The corresponding z distributions of the second fastest particle from the xenon and deuterium targets are compared in Fig. 17, for both kinematic regions, low and high, while those from the third fastest particle are compared in Fig. 18. The ratios indicate that these distributions are also consistent between the two targets, for both regions of kinematics.

B. Steepening with order

In comparing the z distributions for the first three fastest charged particles, it is clear that they steepen with increasing order. We can quantify this by examining the slope values from the exponential fits, described by Eq. (25). If we focus on the data from the deuterium

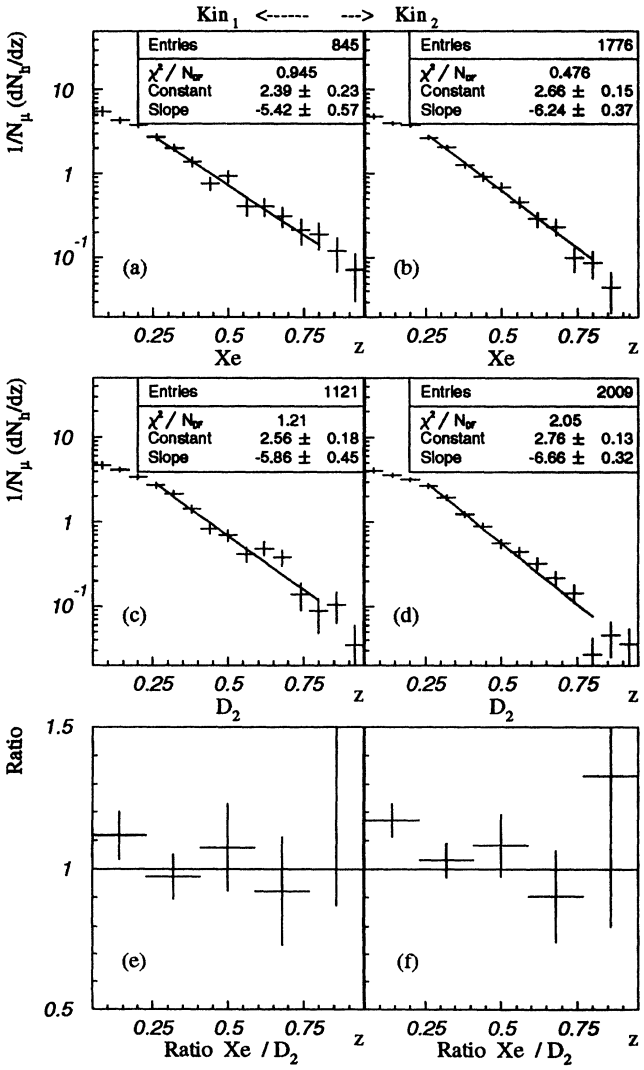

FIG. 16. z_1 distributions: Xe and D_2. These plots show the z-distributions of the fastest particles from xenon and deuterium and the ratios of the distributions. The distributions on the left are from events in the low kinematic region: Kin_1, while those on the right are from events in the high kinematic region: Kin_2. The data from these plots are tabulated in Tables XXI and XXXV.

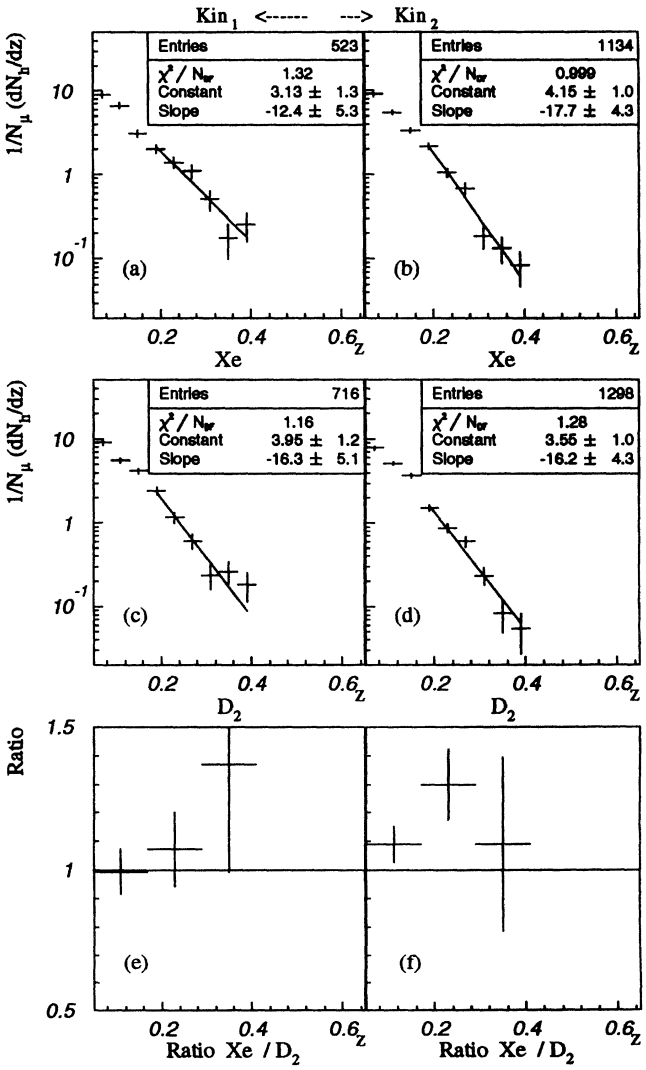

FIG. 17. z_2 distributions: Xe and D_2. These plots show the z distributions of the second fastest particles from xenon and deuterium and the ratios of the distributions. The distributions on the left are from events in the low kinematic region: Kin_1, while those on the right are from events in the high kinematic region: Kin_2. The data from these plots are tabulated in Tables XXII and XXXVI.

Kin_2 sample, the slopes progress from fastest to third fastest as -6.7, -16, and -31.

The steepening of the distributions with increasing order was to be expected, given the known distribution of multiplicity and the kinematic constraints on the z ordering. Let the z distributions of the first three fastest particles be represented by the functions $h_1(z), h_2(z)$, and $h_3(z)$, which are defined on the intervals $(0,1), (0,1/2)$, and $(0,1/3)$, respectively. Then, the mean numbers of particles produced with these respective orders are given by the integrals of the three curves:

$$\langle n_1 \rangle = \int_0^1 h_1(z)dz, \tag{40}$$

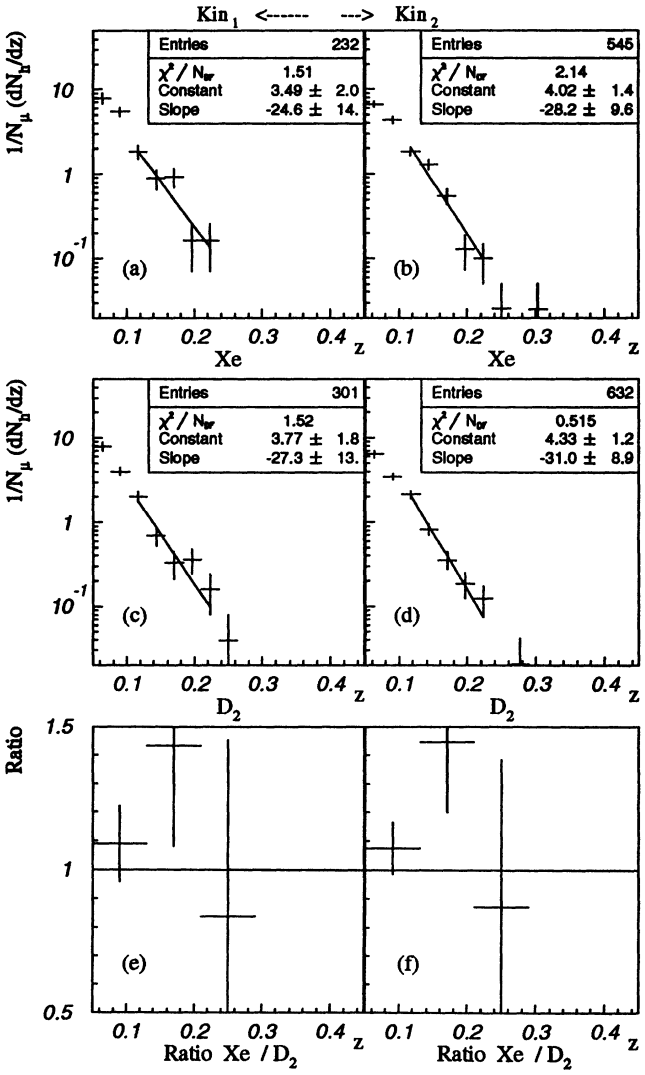

FIG. 18. z_3 distributions: Xe and D_2. These plots show the z-distributions of the third fastest particles from xenon and deuterium and the ratios of the distributions. The distributions on the left are from events in the low kinematic region: Kin_1, while those on the right are from events in the high kinematic region: Kin_2. The data from these plots are tabulated in Tables XXIII and XXXVII.

$$\langle n_2 \rangle = \int_0^{1/2} h_2(z)dz, \tag{41}$$

$$\langle n_3 \rangle = \int_0^{1/3} h_3(z)dz. \tag{42}$$

If the distribution of the second-ordered particles were to have the same shape as that of the first-ordered particles, then the functional representations should differ only by a scale factor. Since all three distributions must vanish as z approaches the upper limit of the kinematically allowed range, somewhere near the upper limits the rates must have similar values; this sets the size of the scale factor. If all three distributions had a functional form proportional to e^{-6z}, then the scale factor between the order-2 and order-1 particles would be $(1/20)$; the scale factor between the order-3 and order-1 particles would be $(1/55)$.

Empirically, the multiplicity distribution does not fall off nearly this quickly. There are many more order-2 and order-3 particles than indicated by the hypothesis of similarly shaped distributions. Therefore, since the upper limits of the distributions are fixed, the slopes must steepen to increase the mean production of particles and, thus, to increase the area under the curve.

C. Rescaled z

The steepening is caused by the multiplicity and the kinematic constraints. The kinematic constraints can be removed by rescaling the energy of each hadron by the energy available to *it*, progressing down the ordering in z. Thus, the energy of the second fastest is scaled to the energy available to it, by Eq. (6). Similarly, the energy of the third fastest is scaled to the energy available to it, by Eq. (8).

We compared the distributions of the rescaled-z variables between xenon and deuterium. These rescaled-z distributions for the low kinematic range are shown in Fig. 19, with those from xenon on the left and deuterium on the right. The distributions for the high kinematic range are displayed in Fig. 20. It is apparent that the slopes of these distributions for the fastest three charged particles are consistent within the experimental errors, although there is a residual trend to steepen, which we will discuss in the next section. It is also evident that the distributions for a given target are consistent across the two kinematic regions.

The ratios of these rescaled distributions (z_2 and z_3) of xenon over deuterium are shown in Fig. 21, for both kinematic ranges; in both sets the ratios are consistent with unity. The ratios of the distributions in z_1 have been shown in Fig. 16.

D. Rescaled z with z_{sum} cut

In the analysis of the rescaled-z distributions, only reconstructed charged particles contributed, so there was some contamination in each distribution from the "shuf-

fling" of the particles. Neutral particles and charged particles whose tracks failed reconstruction were missing from the ordering, so the next reconstructed order particles shuffled up into their positions. We attempted to eliminate this contamination from the rescaled distributions by requiring that each event had sufficient reconstructed energy to rule out a missing intermediate particle from the ordering, using the sum of z of the reconstructed charged particles defined by the following:

$$z_{\rm sum} \equiv \sum_{\rm ch} z_{\rm ch}. \tag{43}$$

The maximum z value that a missing particle could have was given simply by $z_{\rm lost} = (1 - z_{\rm sum})$. Therefore, if $z_1 > z_{\rm lost}$ there could not be a missing particle which should have been ordered as the fastest particle. Similarly, if $z_2 > z_{\rm lost}$ there could be no missing intermediate particle between those defined as the fastest and the second fastest, and if $z_3 > z_{\rm lost}$ there could be no missing intermediate particle between those defined as the second fastest and the third fastest.

The rescaled-z distributions with the $z_{\rm sum}$ restrictions are shown in Fig. 22 as the diamonds, overlaid on the unrestricted distributions, the simple crosses. The distributions from xenon are on the left, while those from deuterium are on the right. (These distributions include the full kinematic range, defined by the "final kinematic

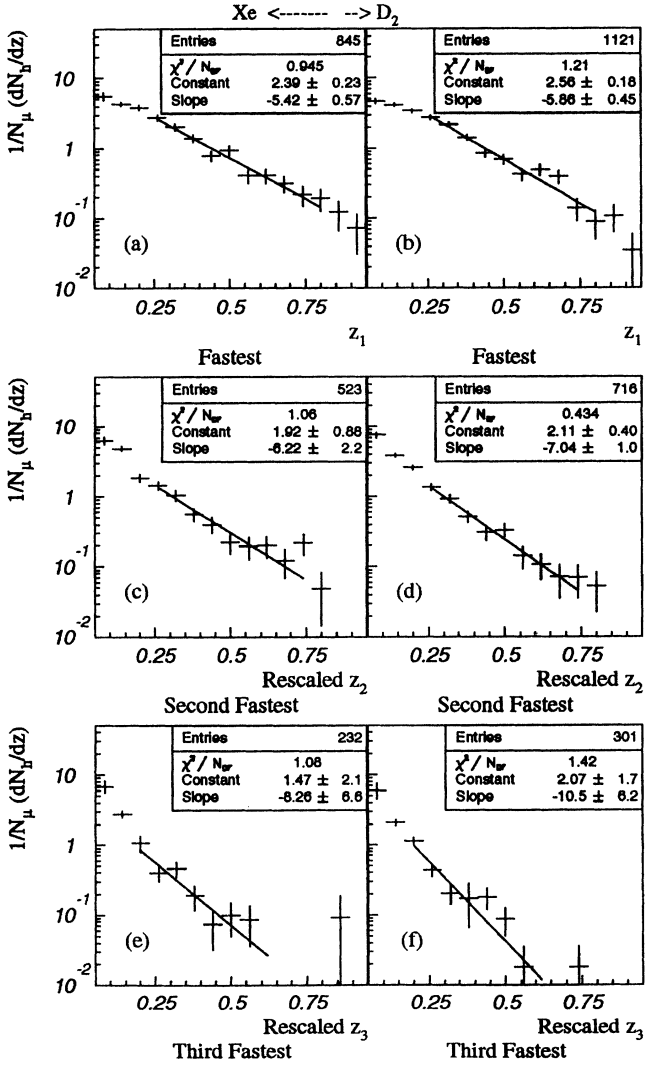

FIG. 19. Rescaled-z values, low kinematics. These plots show the distributions of the rescaled-z values for xenon (a,c,e) and deuterium (b,d,f). In (a) and (b) are the distributions for the highest z track; the rescaling has no effect on these values. In (c) and (d) are the distributions of the rescaled-z values for the second highest z tracks. In (e) and (f) are the distributions of the rescaled-z values for the third highest z tracks. The rescaled data from these plots are tabulated in Tables XXIV and XXV.

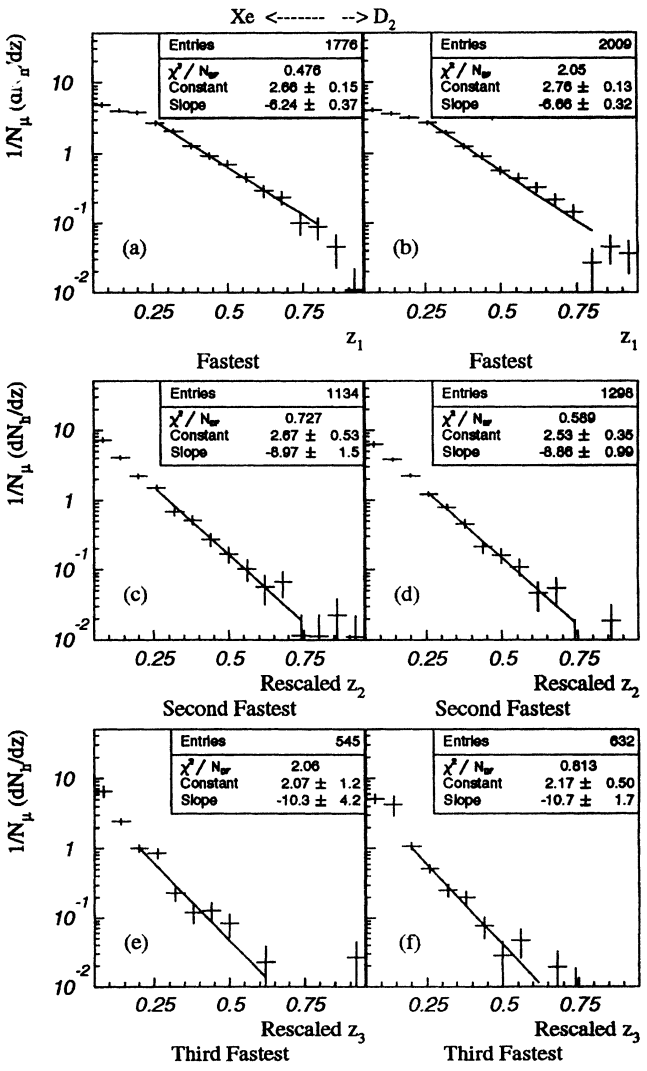

FIG. 20. Rescaled-z values, high kinematics. These plots show the distributions of the rescaled-z values for xenon (a,c,e) and deuterium (b,d,f). In (a) and (b) are the distributions for the highest z track; the rescaling has no effect on these values. In (c) and (d) are the distributions of the rescaled-z values for the second highest z tracks. In (e) and (f) are the distributions of the rescaled-z values for the third highest z tracks. The rescaled data from these plots are tabulated in Tables XXIV and XXV.

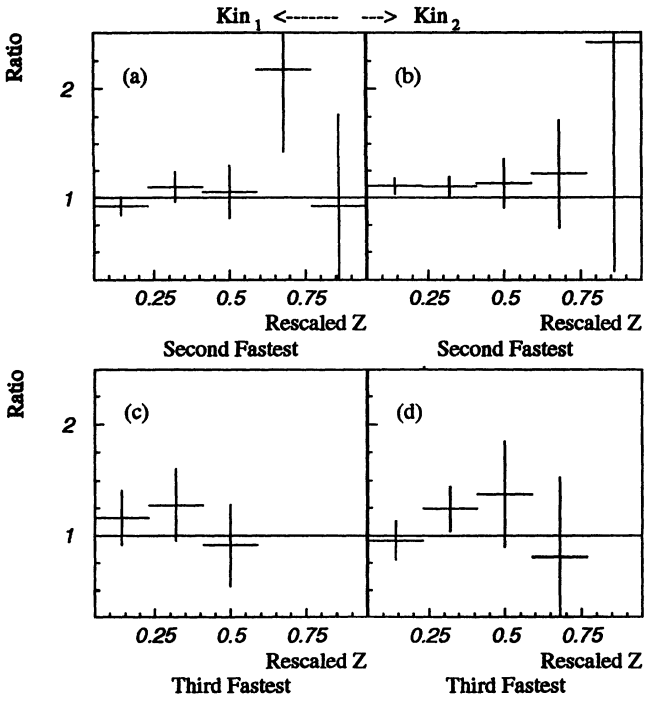

FIG. 21. Ratios of Xe/D_2 rescaled-z distributions. These plots show the ratios of the rescaled-z distributions of xenon over deuterium. On the left are the ratios for the low kinematic region: Kin_1; on the right are the ratios for the high kinematic region: Kin_2. The ratios on the top row are for the rescaled-z_2 particles, while those on the bottom are for the rescaled-z_3 particles. The data from these plots are tabulated in Tables XXXVIII and XXXIX.

cuts" in Table IX). The low-z end of the restricted distributions is cut off due to the $z_{\rm lost}$ cut, which is effectively a minimum-z cut. For values of z greater than 1/2, clearly this cut has no effect. The exponential fit has been performed on this "unambiguously ordered" region, and the results are included in the plots.

There is some evidence that these distributions, especially that of z_3, have different slopes on either side of $z = 1/2$. It is likely that the steeper slope at low z is caused by the contamination of the sample by the shuffling effect. The slope on the high-z side, however, can be compared between the orders. It is apparent that these slopes of the distributions for the fastest three charged particles are all consistent within the errors. This is suggestive of some fundamental process involved in the fragmentation that results in this characteristic distribution.

We have combined the data from the first three fastest particles for the whole kinematic range, separately for both the xenon and deuterium targets. These distributions are plotted in Fig. 23 as functions of the rescaled-z variables. The distributions from xenon are on the left, while those from deuterium are on the right. The samples including only those hadrons which satisfy the $z_{\rm sum}$ restriction are shown as the diamonds, overlaid on the unrestricted distributions, the simple crosses. The exponential fits of the upper z regions are consistent between the two targets.

E. Evaluation of ordering

To discuss the significance of the scaling, we refer to the Feynman-Field-Fox work of Ref. [33]. They assume *a priori* that the formation of the "primary mesons" would proceed in a scaled fashion. Our data distributions from the successive z orderings are consistent with a single parent distribution. This parent distribution can be taken as the analogue of the probability function of fragmentation chain hierarchy, $F(z)$ [33]; however, in our case the parent distribution is ordered according to the physically observable z and not to position in the fragmentation chain. The scaling of the data distributions of the observable quantity is information additional to the as-

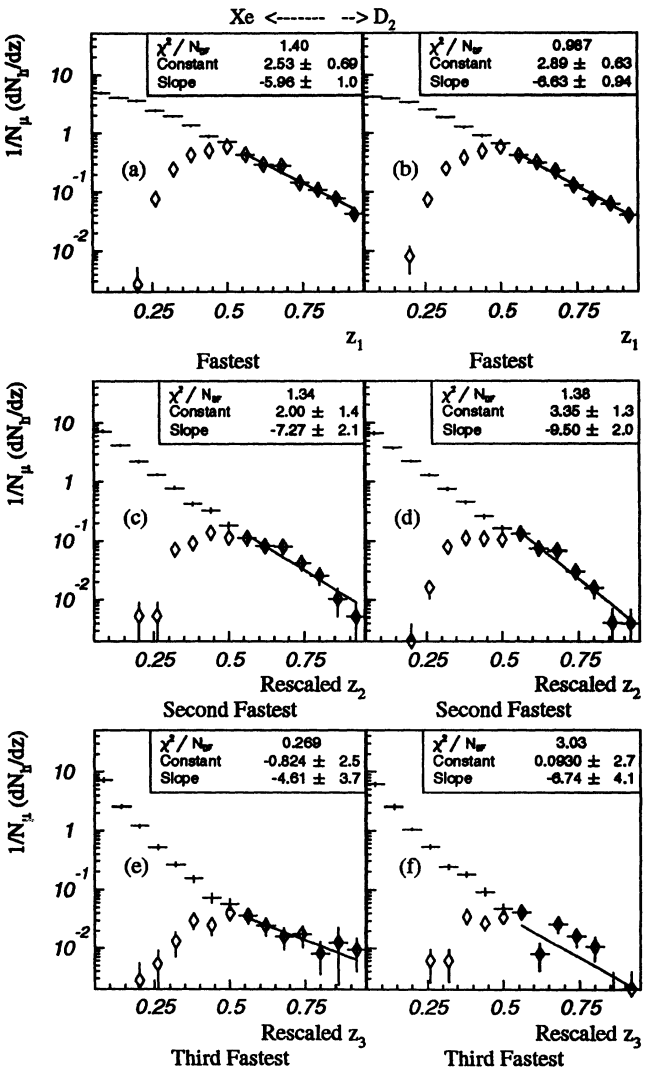

FIG. 22. Rescaled $z > z_{\rm lost}$. These plots show the distributions of the rescaled-z values for xenon (a,c,e) and deuterium (b,d,f); the diamonds represent the distributions with contributions only from tracks with $z_i > z_{\rm lost}$. In (a) and (b) are the distributions for z_1; in (c) and (d) are the distributions of the rescaled z_2, while in (e) and (f) are the distributions of the rescaled z_3. These plots include data from the full kinematic range; the data are tabulated in Table XXVI.

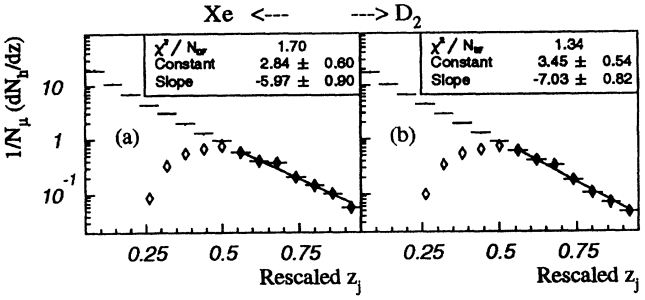

FIG. 23. Rescaled $z_j > z_{\rm lost}$, $j \in \{1,2,3\}$. These plots show the distributions of the rescaled-z values for xenon and deuterium, with contributions from tracks with $z_j > z_{\rm lost}$, where $j \in \{1,2,3\}$ indicates that the first three fastest particles are included in the samples. These data include the full kinematic sample; they are tabulated in Table XXVII.

sumptions used in Ref. [33] to describe the rank-hierarchy of primary production. The fact that the data behave well under the ansatz of scaling may indicate a strong correlation between z ordering and production hierarchy.

We have examined this ordering on a sample of LUND (which contains the Feynman-Field-Fox scaling feature) Monte Carlo events, generated for a deuterium target for the full kinematic range. The distributions of the muon-scattering variables were not matched to our data samples, but in the factorization approximation this should not affect the hadron distributions. The plots in Figs. 24(a), 24(c), and 24(e) show the distributions of charged hadrons as functions of the variables z_1, z_2, z_3, respectively. The hadrons in these distributions were restricted to production at the primary vertex but were not required to pass reconstruction; thus, the distributions do not contain the effects of shuffling due to inefficiencies of reconstruction. They do, however, contain the shuffling due to intermediate neutral particles and decays. In Fig. 24(d) the distribution of second fastest charged hadrons is plotted as a function of the variable rescaled z_2, and in Fig. 24(f) the distribution of third fastest charged hadrons is plotted as a function of the variable rescaled z_3. This rescaling was performed, as in the data, using only the energy of the charged hadrons, so the effects of shuffling due to intermediate neutrals are present. The distributions from the Monte Carlo simulation look very much like those from data, including the similarity of the rescaled distributions. This is quantified by comparing the fit results and errors for the normal z with the deuterium results in Figs. 16, 17, and 18 [plots (c) and (d)] and comparing those for the rescaled z with the deuterium results in Figs. 19 and 20 [plots (c) and (d)]. There are no 3σ deviations between the Monte Carlo simulation and the data.

We must point out several caveats to bear in mind in this evaluation. First, we have examined only those hadrons linked to the primary vertex in each event as our approximation to the distribution of production of primary mesons. Second, incidences in which a resonance carries the highest energy fraction and then divides it among its decay products will not contribute directly to the proper z ordering of primary production. A corollary

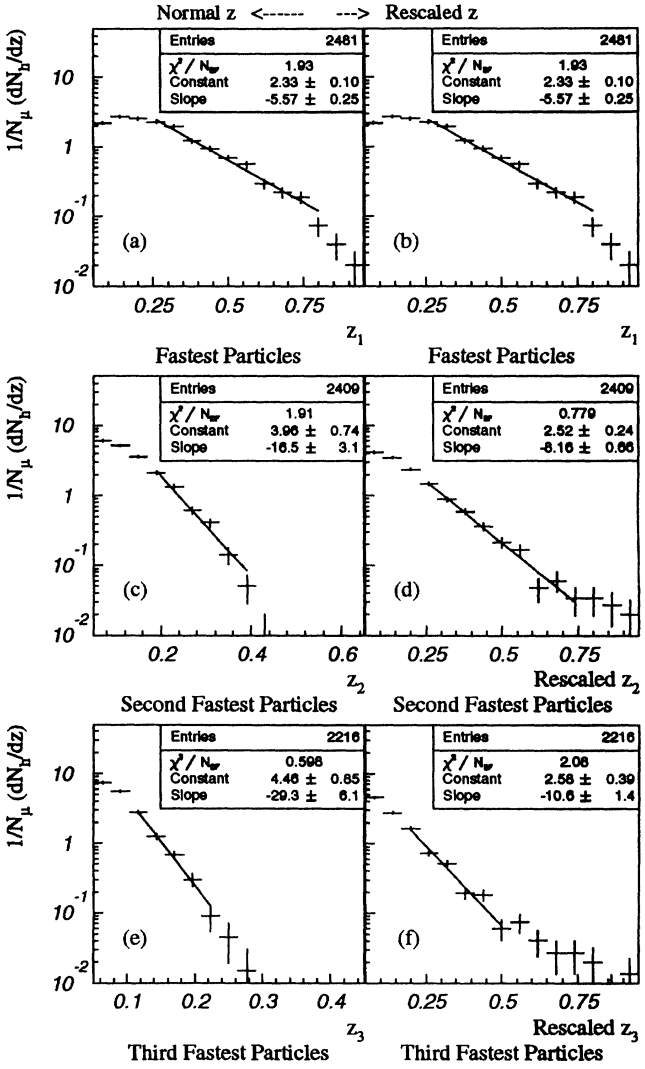

FIG. 24. Monte Carlo rescaled z. These plots show the distributions in z and in the rescaled-z values for a (LUND) Monte Carlo deuterium sample. In (a), (c), and (e) are the distributions of charged hadrons as functions of the variables z_1, z_2, z_3, respectively. In (d) the distribution of second fastest charged hadrons is plotted as a function of the variable rescaled z_2. In (f) the distribution of third fastest charged hadrons is plotted as a function of the variable rescaled z_3. These data are tabulated in Tables XXVIII and XXIX.

to this is that a decay product of a resonance can be mistakenly assigned to primary production, though these decay products will usually fall to lower orderings of z. Finally, we stress that only the unambiguously ordered data distributions yield a valid measurement of primary production ordering.

VII. CONCLUSIONS

We have examined the z distributions of the final state hadrons, comparing scatters from a xenon target to those from a deuterium target. We have examined the distributions in several distinct kinematic regions, in particular

in the region of *shadowing*, where the total cross section exhibits a strong dependence upon the target material and where hadron studies have not been performed previously. These z distributions of the final state hadrons have shown no dependence on the target, even in the kinematic regime of shadowing; the ratios of the distributions from xenon to deuterium are consistent with unity. In addition, the distributions show little discernable dependence on the event kinematics.

Our data are from events with large energy transfer, ν; an analysis of low-ν scatters may be found in Ref. [34]. We have assumed that all of the final state hadrons form outside of the nucleus and that they cannot, therefore, be attenuated by the nucleus; our data are consistent with this assumption. If the struck quark were attenuated due to its traversal of the nuclear matter in a nucleus, then the resultant final-state z distribution should "steepen." For a hadronlike interaction, the fractional probability of such a postulated rescattering in the xenon nucleus would have had a value of $I = 0.87$; our data indicate that this fractional probability is less than $I = 0.164$, at the 95% confidence level. From these examinations of the z distributions it appears that there is little attenuation of the struck-quark system traversing nuclear matter. Consequently, the production of final state hadrons in muon-nucleus scattering is different than in hadron-nucleus scattering. It would be interesting to search for nuclear dependence in the nondiffractive channel of real photoproduction, in which Q^2 is exactly zero.

We have made several observations based upon the ordering of the hadrons according to their energy fractions. The single-particle distributions of similarly z-ordered hadrons appear to belong to the same parent distribution, regardless of the target material or of the event kinematics. In defining a variable which scales the energy of a given final state hadron to the energy available to that hadron, we have observed that the differential rate of production of a hadron, as a function of this variable, looks similar for all hadrons in the forward region of the fragmentation chain. This suggests that the shape of the distribution is related to some fundamental property of fragmentation.

ACKNOWLEDGMENTS

We wish to thank all those personnel, both at Fermilab and at the participating institutions, who have contributed to the success of this experiment. The work of Fermi National Laboratory was supported by the Department of Energy under Contract No. DE-AC02-76CHO3000. The work of the University of California, San Diego was supported in part by the National Science Foundation, Contract Nos. PHY82-05900, PHY85-11584 and PHY88-10221; the University of Illinois at Chicago by NSF Contract No. PHY88-11164; and the University of Washington by NSF Contract Nos. PHY83-13347 and PHY86-13003. The University of Washington was also supported by the U.S. Department of Energy. The work of Argonne National Laboratory was supported by the Department of Energy, Nuclear Physics Division, under Contract No. W-31-109-ENGGG-38. The Department of Energy, High Energy Physics Division, supported the work of Harvard University, the University of Maryland, the Massachusetts Institute of Technology under Contract No. DE-AC02-76ER03069 and Yale University. The Albert-Ludwigs-Universität and the University of Wuppertal were supported in part by the Bundesministerium für Forschung and Technologie.

APPENDIX A: DATA SELECTION AND CORRECTION

This section discusses examinations of the effects of possible systematic errors [2]. The events used in this analysis were taken on two targets, deuterium and xenon, and were based on two triggers, LAT and SAT, as described in Sec. A 7. Since the triggers depended mainly upon the incoming and scattered muons, no strong dependence of the hadrons upon the triggers should be expected; however, to justify merging the samples from these two triggers, we show that no bias on the hadron distributions was introduced by the trigger requirements. Also, we detail the examination of the background and the set of "cuts" developed to limit the contamination of the hadron distributions by this background. The methods used to correct the data for acceptance are discussed in Sec. A 6.

1. Systematic error

From our examination of possible systematic uncertainties, which we detail below, we estimate the systematic error on the z distributions, corrected for rescattering, to be less than 10%, above $z = 0.2$. The error on the deuterium distributions before correction for rescattering is 14%, above $z = 0.2$. The acceptance corrections become quite large for low-momentum tracks ($\sim$ 50%), which increases the systematic uncertainty on the distributions for z values below about 0.2. We estimate the systematic error on the distributions for $z < 0.1$ to be as much as 20%; we have, therefore, excluded this region in the quantitative comparisons.

2. z resolution

For examining distributions of z it is important to understand the resolution with which the values are calculated. The fractional error on z is determined from Eq. (4) and can be written

$$\frac{\Delta z}{z} = \sqrt{\left(\frac{\Delta \nu}{\nu}\right)^2 + \left(\frac{\Delta E_h}{E_h}\right)^2}. \tag{A1}$$

Obviously, the resolution on z will depend upon that of ν; the fractional resolution on the measurement of ν can be seen in Fig. 25, for the deuterium sample of events. The energy exchange ν is calculated from the difference of the incident and outgoing muon energies, and the track

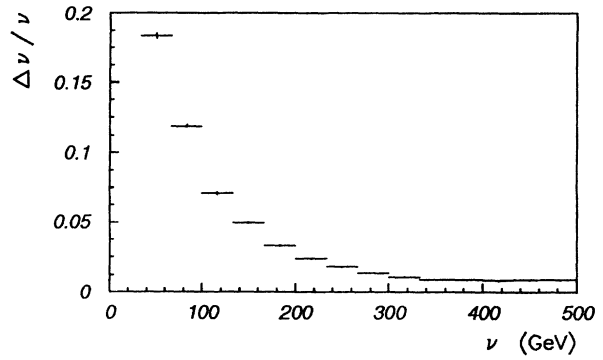

FIG. 25. ν resolution. This plot shows the resolution on ν, $\Delta\nu/\nu$, as a function of ν.

measurement uncertainties are propagated to derive $\Delta\nu$. Since ν is the difference between two numbers, the fractional uncertainty increases for lower energy exchanges. This is clearly visible in Fig. 25.

In order to keep the resolution of the distributions of z reasonable, we have chosen to restrict the sample of events to those with reasonable resolutions on ν, using the criterion $100 < \nu < 500$ GeV. In Fig. 26, the resolution plots of z now have this restriction applied and are shown distinctly for three ranges of kinematics: Kin_1, Kin_2, and *overlap*. The first two are defined by Eqs. (22) and (23), while the overlap region is defined by the following kinematic restrictions:

$$\text{overlap} \equiv \begin{cases} 0.01 < x_{\text{Bj}} < 0.3 \\ 1 < Q^2 < 10\ \text{GeV}^2/c^2. \end{cases} \quad \text{(A2)}$$

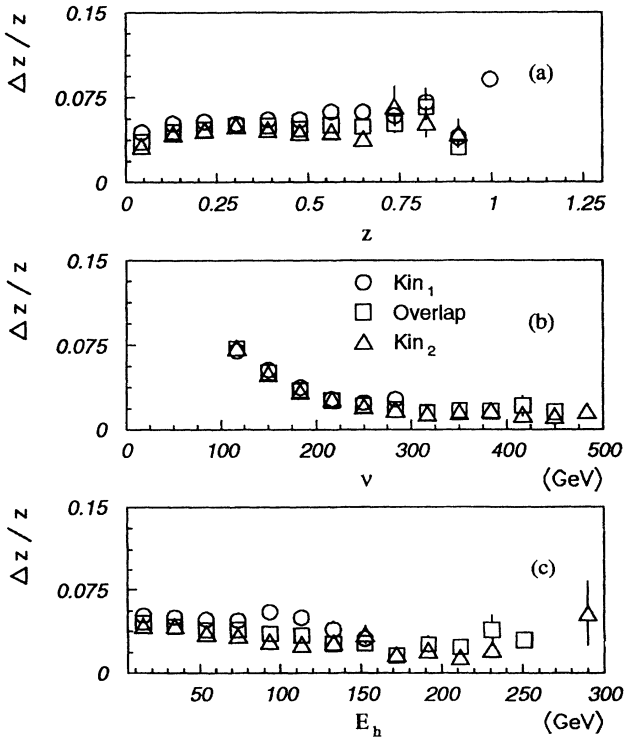

FIG. 26. z resolution, $100 < \nu < 500$ GeV. These plots show the resolution on z as a function of its dependent variables: E_h and ν, but with a restricted range of ν values. $\Delta z/z$ is plotted as a function of z in (a), of ν in (b), and of E_h in (c); for each plot, three ranges of Q^2 and x_{Bj} are shown overlaid.

It is evident that the resolution on z is consistent for all three ranges of kinematics.

There were a few tracks in the samples which were unphysical, i.e., had z values greater than 1; there were also tracks which were second highest in energy but which had energies greater than 0.5ν. We attempted to understand the source of these tracks and to devise cuts which would reject them. These unphysical tracks appear to have characteristically poor resolution. With a z resolution of 10%, one would expect to find z values out to about 1.1 or thereabout. After we rejected the tracks with poor energy resolution, $\Delta E_h/E_h > 0.1$, and unphysical energies, $E_h > 1.2\nu$, the z distributions for the fastest, the second fastest, and the third fastest hadrons each had very little leakage above its respective physical barrier of 1.0, 0.5, and 0.33. The few tracks which failed these quality cuts appeared to be extra beam muon tracks.

A lack of resolution would smear out the distribution in z. Since the distribution drops roughly exponentially with increasing z, the smearing would result in entries from the z_i bin "spilling down" into the z_{i+1} bin, which would flatten out the histogram of the parent distribution. Since the fractional error on z is constant as a function of z, as evidenced from Fig. 26(a), the smearing will have the largest effect at high z. We estimate this systematic error at high z to be less than 3%. A systematic shift in the momentum and energy measurements would also shift the z distributions; we estimate this systematic error to be less than 8%.

3. Event selection

a. *Targets*

The experiment took data scattered from both deuterium and xenon. The target vessels resided inside the streamer chamber, which required that all target material be nonmetallic. The vessel used for the liquid deuterium target was 8.9 cm in diameter and 115 cm long and was constructed of 1 mm thick Kapton. The xenon was a high pressure (14 atm) gaseous target, and the vessel was constructed of Kevlar™ and epoxy, 1 mm in thickness; this vessel had a diameter of 7.2 cm and a length of 113 cm. Information about the targets is listed in Table VIII.

The deuterium target was almost 1/3 of a nuclear interaction length and 1/4 of a pion-interaction length; corrections for the reinteraction of hadrons produced in deep-inelastic scatters were discussed in Sec. IV. The xenon target was almost a full radiation length of material, and this resulted in increased incidence of muon-electron scattering and muon-bremsstrahlung events over the lighter target.

TABLE VIII. E665 target properties. Z is the atomic number and A is the atomic weight. The L_R value is the fraction of radiation lengths in the target, while the L_D value is the fraction of nuclear interaction lengths. We take L_π to represent the length of the target in terms of the π-deuterium inelastic scattering.

Target	Z/A	Length (cm)	Diameter (cm)	Density (g/cm^3)	L_R	L_D	L_π
Xe	54/131.3	113	7.1	0.085	1.00	0.05	0.044
D_2	1/2.0	115	8.9	0.162	0.13	0.312	0.225

b. Triggers

There were two physics triggers implemented in E665: the large angle trigger (LAT) and the small angle trigger (SAT). Their names indicate the major differences in their respective designs. The LAT had angular acceptance down to about 3 mrad, which corresponded to a minimum Q^2 of about 2.7 (GeV/c)^2. The SAT had angular acceptance down to about 1 mrad and a minimum Q^2 of about 0.5 (GeV/c)^2 for full acceptance. The SAT was restricted to take only 12% of the beam phase space used for the LAT.

c. Event rejection

After reconstruction of events, the four data samples, deuterium (SAT), deuterium (LAT), xenon (SAT), and xenon (LAT), were subjected to a set of rejection cuts; the effects of these cuts are summarized in Table IX. The initial event samples contain those events with a reconstructed beam muon, a reconstructed scattered muon, and a reconstructed event vertex, with some minimal requirements on kinematic quantities. First, events were removed from periods which had poor detector performance. The next operation was to remove the events from the LAT sample which satisfied both triggers SAT and LAT, to avoid double-counting them. The events which contained more than one incoming muon in the beam spectrometer were eliminated. The major rejection occurred due to the application of the initial kinematic cuts, listed in Table IX.

In order to reduce the contamination of diffractive meson production, the following criteria were employed. If an event had two and only two charged hadron tracks and these tracks were of opposite charge and carried greater than 90% of the energy transferred, then the invariant mass was calculated; if this mass was determined, within errors, to be that of the ρ^0 (0.770 ± 0.2 GeV) or the ϕ (1.020 ± 0.2 GeV) or the photon (0.0 ± 0.2 GeV), then the event was rejected. The reconstructed event vertex was required to have a fit with a χ^2 probability greater than 0.1%.

For this analysis, no radiative corrections have been applied; instead, a sample of deep-inelastic-scattering events was chosen with a limited level of contamination due to muon-electron scattering and muon-bremsstrahlung radiation. These electromagnetic events would yield apparent kinematic values primarily at high y and low $x_{\rm Bj}$; the μ-e scattering events yield an apparent value of $x_{\rm Bj} = 5 \times 10^{-4}$. Thus, the maximum y-cut and minimum $x_{\rm Bj}$-cut eliminate much of this contamination, but some should remain throughout the full kinematic range. To reduce this remaining contamination, we ap-

TABLE IX. Event selection. This table indicates the number of events rejected by each listed cut. The cuts are listed in the order of their application to the data. The final number of events surviving all cuts is listed at the end for each target and trigger.

Sequence of cuts	D_2(SAT)	D_2(LAT)	Xe(SAT)	Xe(LAT)
Initial number of events	72652	31546	216860	32398
Poor detector performance	7127	2054	13707	2506
Events satisfying both LAT and SAT		3235		2966
Multiple incoming beams	5337	1201	16951	1590
Initial kinematic cuts: $50 < \nu < 550$, $y < 0.8$, $x_{\rm Bj} > 0.0007$, $Q^2 > 0.01$	49934	10194	174291	12552
Diffractive removal	196	136	237	137
χ^2 probability of vertex < 0.001	79	88	138	73
Events cut by CALCUT-1	172	248	326	269
CALCUT-2: $N_{\rm clus} < 3$	1682	912	3652	1356
Final kinematic cuts: $100 < \nu < 500$, $y < 0.75$, $x_{\rm Bj} > 0.001$, ($Q^2 > 1$ or $y < 0.5$), $-11.6m < X_{\rm vertex} < -10.6m$	4872	5757	4716	4733
Final number of events	3253	7721	2842	6216

plied an event rejection based on a set of calorimeter measurements. The energy deposited in the calorimeter was defined to be the sum of the energies of the clusters found in the calorimeter, which had more than 2 GeV each. If this energy was greater than 90% of the energy transferred in the event, then the event was rejected. This is listed in Table IX as CALCUT-1. If the event survived this cut, then a more sophisticated topology was investigated; if the event had only one or two valid clusters found in the calorimeter which summed to more than 50% of the energy transferred, then the event was rejected. In Table IX this cut is listed as CALCUT-2. A comparison of radiative corrections and calorimeter rejection techniques can be found in Ref. [6].

Finally, a set of kinematic cuts was applied. The numbers of events remaining after these rejections are listed in Table IX. Further details about the event selection may be found in Ref. [2].

d. Event losses from π^0 in the calorimeter

The number of events rejected by the calorimeter cuts due to π^0 from deep-inelastic scattering events should be less than about 2.5%. This estimate was based on the following evaluation. The probability of producing a charged hadron with fractional energy of the event greater than a half is given by the integral over the differential cross section for hadron production:

$$P(z > 1/2) = \frac{\int_{\frac{1}{2}}^{1} e^{-bz} dz}{\int_{0}^{1} e^{-bz} dz}. \tag{A3}$$

With the generic value of $b = 6$, the probability is roughly 5%. π^0 production is about half of that of charged pions [35]; conversion of the two decay photons into electron-positron pairs and acceptance for the members of the pairs in the calorimeter reduces the probability below 2.5%.

4. Track rejection

We imposed some quality cuts on the tracks selected. These cuts are listed in Table X. To be included in the initial sample, a track had to have a sufficient number of hits. Since this study concerned the fastest particles from hadronization and the effects of nuclear matter on their formation, we only considered particles propagating from the primary vertex. The determination of whether or not a track should be *fitted* to the primary vertex was left to the vertex processor. Further details about the track selection may be found in Ref. [2].

5. Calorimeter cuts

a. Bremsstrahlung contamination

The extent to which the calorimeter cuts biased the resultant data samples can be examined by looking at some distributions for the events which have been cut by the calorimeter rejection. These distributions are shown in Figs. 27–29, with the events which survived the calorimeter cuts shown on the left and those which were rejected by the calorimeter cuts shown on the right. The sample of xenon SAT events was used for the distributions, since it should contain the most contamination of electromagnetic processes, because of the large charge of the xenon nucleus and the high acceptance of those triggers for small angle scatters.

It is evident from the kinematic distributions for ν, Q^2, x_{Bj}, W^2, and y that the rejected events are characteristically different from deep-inelastic scattering. From the "$\log_{10} Q^2$ versus $\log_{10} y$" plots in Fig. 28 it is clear that the rejected events fall primarily in the region in which radiative processes dominate. The use of a minimum cut of $x_{\mathrm{Bj}} > 0.001$ reduces the contamination of muon-electron scattering and muon-bremsstrahlung radiation. The slanted line on the plots indicates the contour of constant x_{Bj} for our mean beam energy of 490 GeV. The rms spread of the beam energies was 50 GeV, and we had beam energies between 200 and 800 GeV; consequently, the cut of $x_{\mathrm{Bj}} > 0.001$ does not follow this line for all events. In addition to using this x_{Bj} cut, we removed a bit more of the "corner" of the plot in Fig. 28; specifically, we kept the event only if

$$x_{\mathrm{Bj}} > 0.001 \ \text{AND} \ \left(Q^2 > 1\ \mathrm{GeV}^2/c^2 \ \text{OR} \ y < 0.5\right). \tag{A4}$$

In Figs. 29(a) and 29(b), the z distributions indicate

TABLE X. Track selection. This table indicates the number of tracks rejected by each listed cut. The cuts are listed in the order of their application to the data. The final number of tracks surviving all cuts is listed at the end for each target and trigger.

Track cuts	D_2(SAT)	D_2(LAT)	Xe(SAT)	Xe(LAT)
Initial number of tracks	9715	25464	8351	20360
Failed fit	418	994	342	886
χ^2 probability < 0.001	296	834	273	725
Not fitted to a vertex	1808	5030	1618	4161
Not primary vertex	955	3216	850	2416
$\Delta E/E > 0.1$	32	125	40	91
$E > 1.2\nu$	2	1		2
Final number of tracks	6204	15264	5228	12079

that the produced charged particles in the rejected events are more evenly distributed in the available energy. This is suggestive of an electron from a γ conversion. The multiplicity distributions, Figs. 29(e) and 29(f), indicate that mainly events with no produced charged particles were rejected and that these events had a different topology than the surviving events. The z and multiplicity distributions for deuterium LAT are shown in Fig. 30. This sample should be the least contaminated with electromagnetic background; the distributions look similar to those from the events surviving the calorimeter cuts. These calorimeter cuts were imposed on the events used in the analysis of the hadronic final states.

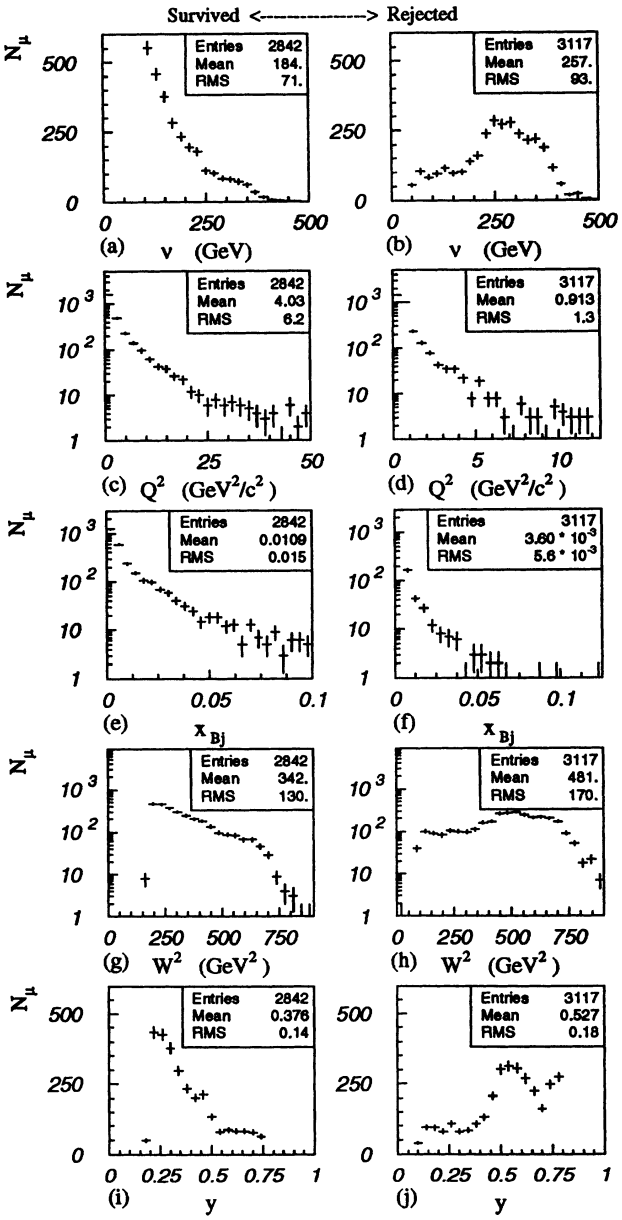

FIG. 27. $\nu, Q^2, x_{\mathrm{Bj}}, W^2, y$, Bremsstrahlung removal. On the left are the distributions from the events which survived the calorimeter restrictions, and the ones on the right are from the events which were rejected by the calorimeter. These data have not been corrected for acceptance.

6. Corrections for acceptance and reconstruction

a. Defining the correction function

To extract the distribution from the physical process of interest from that observed in an experiment, we must account for the influence of the apparatus and the limits of the reconstruction's performance. Throughout the paper, we have called this recovery "correcting the results for *acceptance*." This process can be expressed within the class of integral *Fredholm equations*, where a *Fredholm equation of the first kind* has the form [30]

$$\phi(z) = \int_a^b K(z|z_0)\Phi(z_0)dz_0. \tag{A5}$$

Here $\phi(z)$ is a known function, which corresponds to the

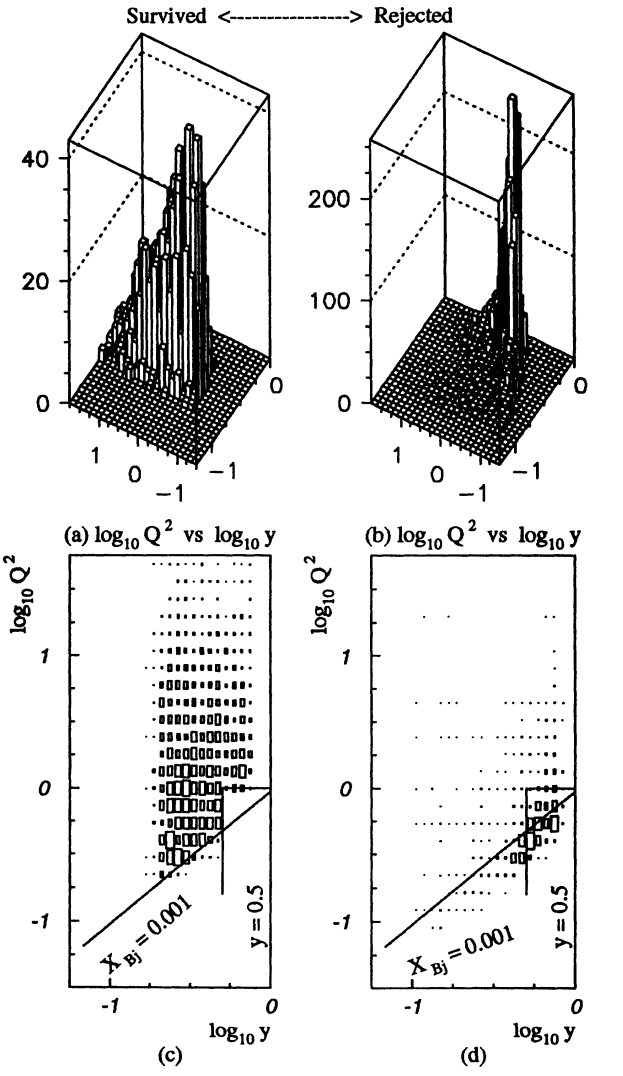

FIG. 28. Q^2 versus y, bremsstrahlung removal. On the left are the distributions from the events which survived the calorimeter restrictions, and the ones on the right are from the events which were rejected by the calorimeter. These data have not been corrected for acceptance.

distribution *observed* in a measurement. $\Phi(z_0)$ is the unknown *true* distribution generated by the physical process. The *kernel* $K(z|z_0)$ maps the function $\Phi(z_0)$ onto the function $\phi(z)$. In order to return to the true distribution $\Phi(z_0)$ from the observed distribution $\phi(z)$ the kernel must be understood and its inverse found. In principle, the kernel may be a function of several variables which are relevant to the distribution in question.

The use of a Monte Carlo program is helpful for determining the relevant kernel, since both the true distribution and the observed distribution are known. Then, for each effect a projection of the kernel onto that variable can be made, and the variables upon which the kernel displays major dependence can be found.

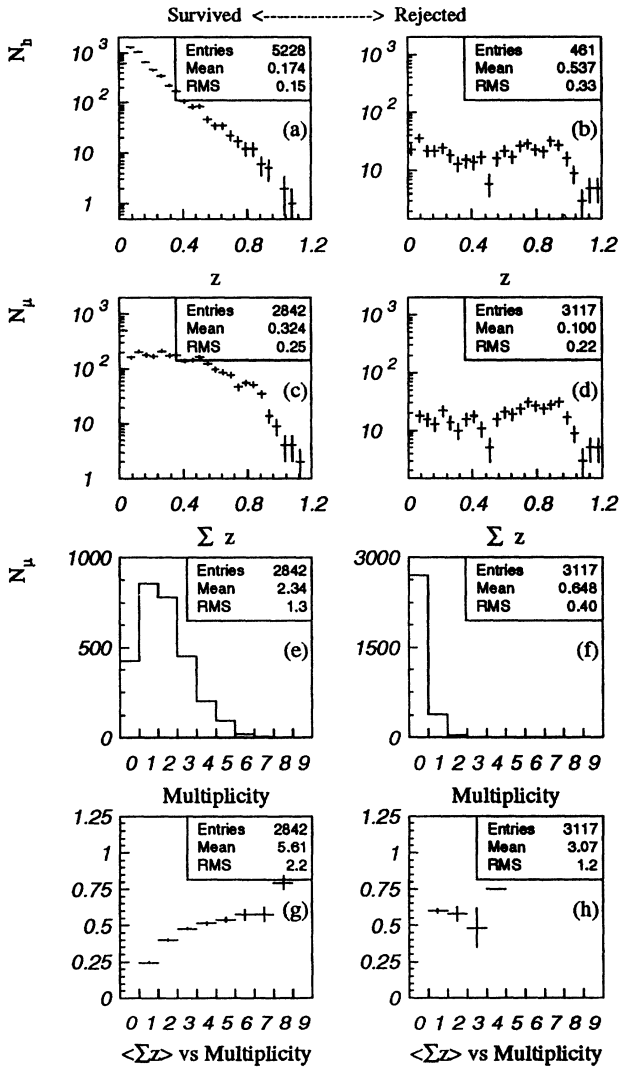

FIG. 29. z and multiplicity distributions, bremsstrahlung removal. On the left are the distributions from the events which survived the calorimeter restrictions, and the ones on the right are from the events which were rejected by the calorimeter. Plots (a) and (b) show the unnormalized z distributions. Plots (c) and (d) show the summed z per event, and (e) and (f) show the multiplicity. Plots (g) and (h) show the mean-value of the summed z per event as a function of the multiplicity. These data have not been corrected for acceptance.

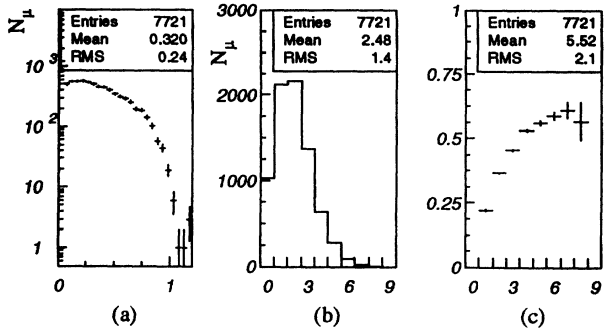

FIG. 30. z and multiplicity distributions of D_2 LAT. Plot (a) shows the summed-z, $\sum z$, per event; (b) shows the multiplicity distribution, and (c) shows the mean value of the summed z per event, $\langle \sum z \rangle$, as a function of the multiplicity. These data have not been corrected for acceptance.

b. Monte Carlo events

We have used Monte Carlo events to map the correction function. For this analysis, events were generated using the LUND program, version 4.3 [10]; a description of the choices of parameters may be found in Ref. [36]. For mapping the correction function, the actual forms of the generated true distributions, $\Phi(z_0)$, must be reasonably similar to those observed in the data, and the detector system must be modeled in great detail, including time-dependent chamber efficiencies.

To indicate the level to which our Monte Carlo program mimicked our detector and the particle trajectories through it, we compare two distributions in Fig. 31. The plot in Fig. 31(a) shows the raw (uncorrected) data distribution as the points with errors; these data are from the full kinematic range from the deuterium target. The histogram overlaid on these data is from fully reconstructed Monte Carlo events. The plot in Fig. 31(b) shows the data distribution corrected for acceptance; the histogram overlaid on these data is from the true Monte Carlo distribution. Comparing these distributions using

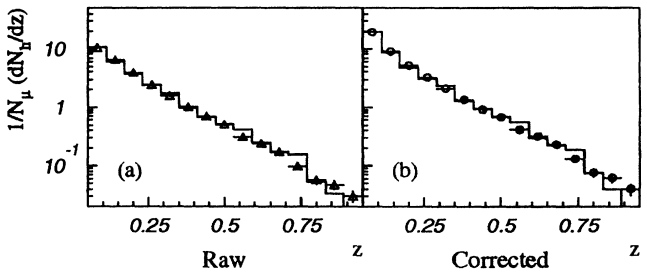

FIG. 31. Monte Carlo simulation compared to data. The plot in (a) shows the raw (uncorrected) data distribution as the points with errors; these data are from the full kinematic range from the deuterium target. The histogram overlaid on these data is from fully reconstructed Monte Carlo events. The plot in (b) shows the data distribution corrected for acceptance; the histogram overlaid on these data is from the true Monte Carlo distribution.

Eq. (31) yields a value of χ^2_A of 0.814 for the "raw" distributions in Fig. 31(a) and of 1.060 for the "corrected" distributions in Fig. 31(b); each comparison was made over the range of z indicated in Eq. (30), resulting in 10 degrees of freedom. The Monte Carlo distributions are sufficiently similar to the data distributions.

c. *Mapping the correction function*

Comparing fully reconstructed Monte Carlo tracks to the true tracks, we examined the dependence of the acceptance upon z, the position and slope of the tracks entering the apparatus, and upon the momentum of the tracks. The acceptance showed the strongest dependence upon the momentum of the tracks and little dependence upon the other variables. Therefore, we defined the basis of the kernel to involve only the one variable, the momentum of the tracks. The detailed examination may be found in Ref. [2(b)].

In comparing the reconstructed tracks to the true tracks, we factorized the acceptance into two components: *fiducial* and *detector* acceptance. The fiducial acceptance involves those tracks which traversed the forward spectrometer, and it was defined by the tracks reaching the first chamber in the momentum-measuring magnet. We collected and analyzed data only inside this fiducial volume. This correction depends upon the geometry of this fiducial and upon the spacial distribution of particles from the events; we must rely upon the Monte Carlo program to describe this particle distribution in order to correct for the fiducial acceptance. This correction is, however, time independent, since it does not depend upon the operation of the detector elements. The acceptance of true tracks from the Monte Carlo tracks into our fiducial volume is shown in Fig. 32, as a function of the energy of the particle; the stiffer, more energetic tracks make it into the detector, with some loss due to hadronic interactions with the material between the target and the detector.

The other component of the acceptance involves the efficiency of the detector recording and reconstructing the track, once it has entered the fiducial volume. This component is fairly insensitive to the actual form of the generated true distributions, but it is dependent upon the time-dependent chamber efficiencies. This detector acceptance is plotted in Fig. 33, again as a function of the particle energy.

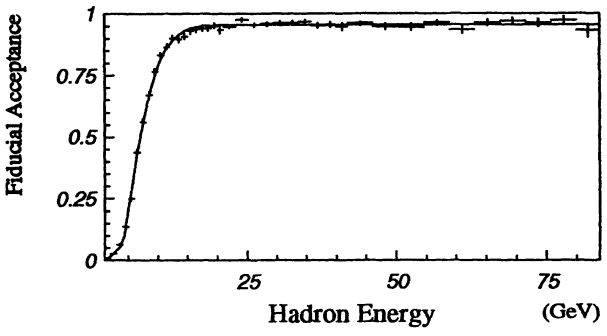

FIG. 32. Fiducial acceptance. This plot shows the acceptance of tracks into the fiducial volume of the detector, as a function of the energy of the tracks. This is the fraction of Monte Carlo true tracks from the primary vertex which pass into the fiducial volume of the detector. The distribution has been fitted to the functional form of Eq. (A6).

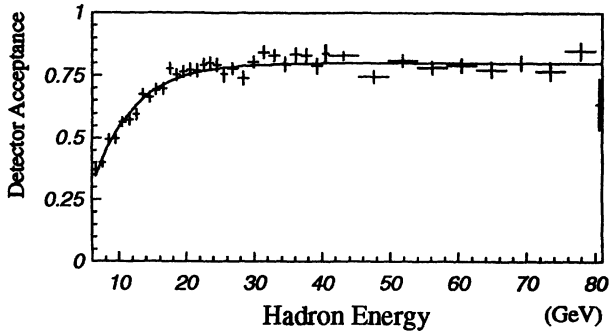

FIG. 33. Detector acceptance. This plot shows the ratio of the reconstructed tracks divided by the true tracks passing into the fiducial volume of the detector, as a function of their energy. The distribution has been fitted to the functional form of Eq. (A7).

The full acceptance of the forward spectrometer (the product of the fiducial and detector acceptances) was poor for low-energy tracks, but leveled out for tracks with energies above 20 GeV. Since the minimum ν was set at 100 GeV, using a minimum value of $z = 0.2$ in quantitative analyses limits the analysis to tracks with energies above 20 GeV, and hence avoids this region of low acceptance.

d. *Smoothing and inverting the correction function*

One possible way to invert the kernel would have been simply to put the inverse of each channels' content into another histogram. However, this scheme is susceptible to statistical fluctuations from bin to bin. Smoothing a distribution for use as a kernel has been discussed in some analyses [37–39]. Choosing to smooth the acceptance function alleviates the dependence on the model of the generation and reduces the number of events which must be generated to obtain sufficient statistical precision so as not to dominate the errors on the corrected distributions.

One technique for smoothing a distribution is to fit a parametrized curve to it. The error from a fitted function is much smaller at a given value of the correction variable than that of a bin of the histogram from the generation itself. We applied this technique to the two acceptance components.

To the fiducial acceptance distribution as a function of the energy of the tracks, shown in Fig. 32, we fitted the parametrization

$$\varepsilon_F(E) = F_1 - (F_2 + F_3E + F_4E^2)e^{-F_5E}, \qquad \text{(A6)}$$

where E was the energy of the track and the F_i were the five parameters of the fit. These parameters are listed in Table XI; the reduced χ^2 from the fit was 1.15.

To the detector acceptance distribution as a function

TABLE XI. Fiducial acceptance. This table contains the values of the parameters from the fits to the fiducial acceptance function, given by Eq. (A6).

F_1	ΔF_1	F_2	ΔF_2	F_3	ΔF_3	F_4	ΔF_4	F_5	ΔF_5
0.957	0.002	1.99	0.13	-0.73	0.14	0.60	0.05	0.577	0.009

of the energy of the tracks, shown in Fig. 33, we fitted the parametrization

$$\varepsilon_D(E) = P_1 - P_2 e^{-P_3 E}, \tag{A7}$$

where E was the energy of the track and the P_i were the three parameters of this fit. The time dependence of the chambers was taken into account in the Monte Carlo simulation, and the parameters are shown as a function of time in Table XII, along with the reduced χ^2 from the fits.

We simply use the product of Eqs. (A6) and (A7) as the definition of the kernel for the acceptance correction. Since the functions $\varepsilon_F(E)$ and $\varepsilon_D(E)$ are analytic in our energy ranges, the inverse kernel was simply

$$K^{-1}(E|E') = \frac{\delta(E-E')}{\varepsilon_F(E)\,\varepsilon_D(E)}. \tag{A8}$$

We applied this correction on a track-by-track basis in the generation of the final z distributions, thus performing the integration of the Fredholm equation (A5).

For tracks with more than about 20 GeV, the correction was essentially a constant value of about 1.31 with an error of about 0.009 for a value of $z \sim 0.5$. This was much less than the errors on the z distributions, so we did not propagate the error from the corrections for acceptance through to the final distributions; this source of systematic error is less than 1%. The effect of smearing the reconstructed z value with respect to the true Monte Carlo z value was small, and we neglect it. The other relevant measure of reconstruction is the fraction of fake tracks created by the software algorithms. We determined this fraction to be less than 2–4%, independent of the z of the track.

TABLE XII. Time-dependent acceptance. This table contains the values of the parameters from the fits to the detector acceptance function, given by Eq. (A7), along with the reduced χ^2 for each fit. The time dependence of the detector acceptance is listed.

Time period	P_1	±	ΔP_1	P_2	±	ΔP_2
D_2 (first)	0.8008	±	0.0055	1.339	±	0.090
D_2 (second)	0.7839	±	0.0050	1.393	±	0.100
Xe (first)	0.7489	±	0.0089	1.289	±	0.130
Xe (second)	0.7369	±	0.0087	1.339	±	0.150
Xe (third)	0.7268	±	0.0094	1.236	±	0.130
Xe (fourth)	0.7415	±	0.0058	1.099	±	0.067

Time period	P_3	±	ΔP_3	χ^2/N_{DF}
D_2 (first)	0.1653	±	0.0081	1.626
D_2 (second)	0.1723	±	0.0086	1.623
Xe (first)	0.1519	±	0.0120	1.080
Xe (second)	0.1679	±	0.0140	1.422
Xe (third)	0.1499	±	0.0120	1.369
Xe (fourth)	0.1366	±	0.0073	1.096

7. SAT and LAT triggers

The two physics triggers implemented in E665, the LAT and the SAT, had different rates and different acceptances. Since the acceptances were different, the kinematic distributions for the two trigger samples were, of course, also different. The raw distributions of event rates, as functions of the kinematic variables Q^2, x_{Bj}, ν, and W^2, are shown for both trigger samples for the deuterium target in Fig. 34 and the xenon target in Fig. 35.

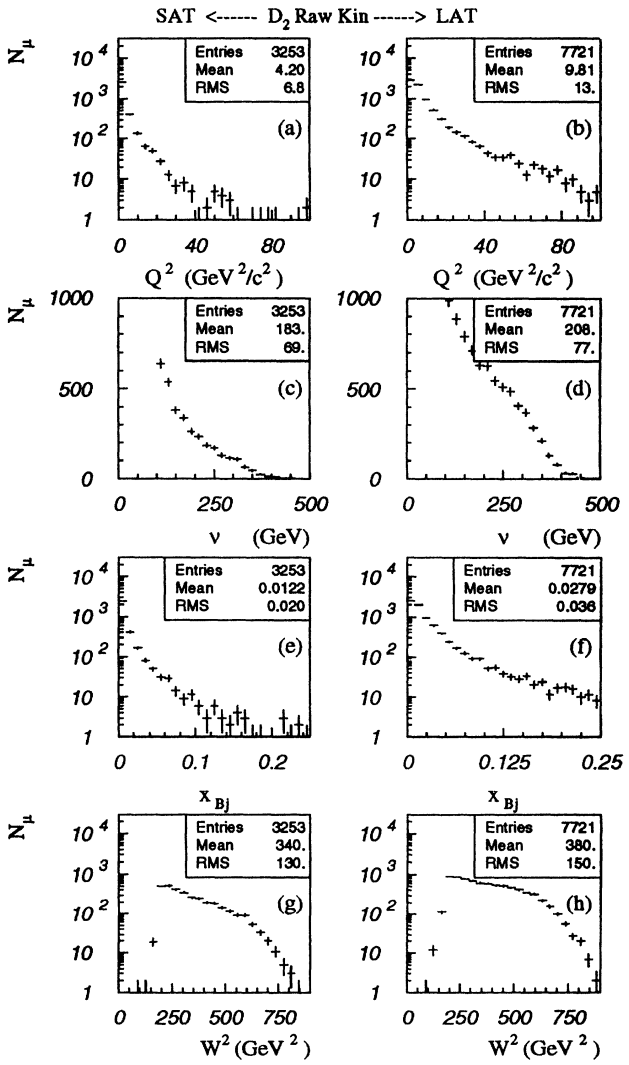

FIG. 34. Raw trigger kinematics for D_2. The plots on the left are from the SAT sample; the plots on the right are from the LAT sample. These data have not been corrected for acceptance but are the raw event rates, after the final kinematic cuts.

These event rates include all those events which survived through the "final kinematic cuts" listed in Table IX. These data have not been corrected for the trigger acceptance or for detector acceptance.

The SAT used hodoscopes in the beam spectrometer to define the beam-muon trajectory and an electronic lookup table to predict where this muon should impinge upon hodoscopes in the muon spectrometer, if it failed to scatter. If these predicted counters fired, then the event was vetoed. This trigger was prescaled to take only 12% of the beam phase space used for the LAT.

The LAT used the beam hodoscopes only to define the timing of the beam muons. It required hits in the outer hodoscopes in the muon spectrometer in three of the four stations for a valid trigger. In addition, however, the event was vetoed if there were hits in beam region hodoscopes in the muon spectrometer. More details concerning the triggers can be found in Ref. [1].

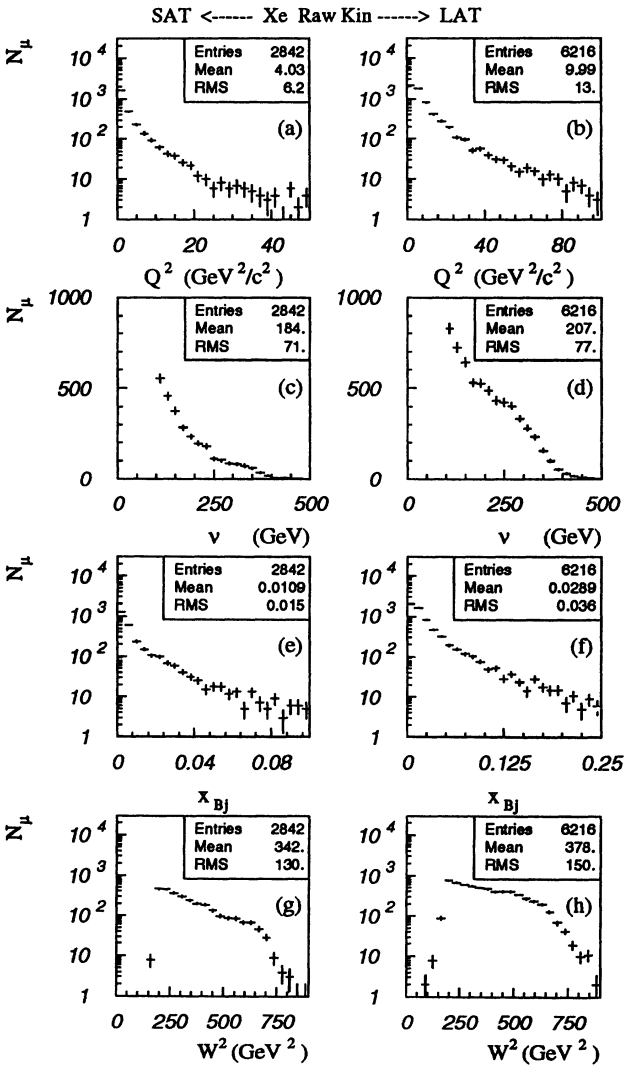

FIG. 35. Raw trigger kinematics for xenon. The plots on the left are from the SAT sample; the plots on the right are from the LAT sample. These data have not been corrected for acceptance but are the raw event rates, after the final kinematic cuts.

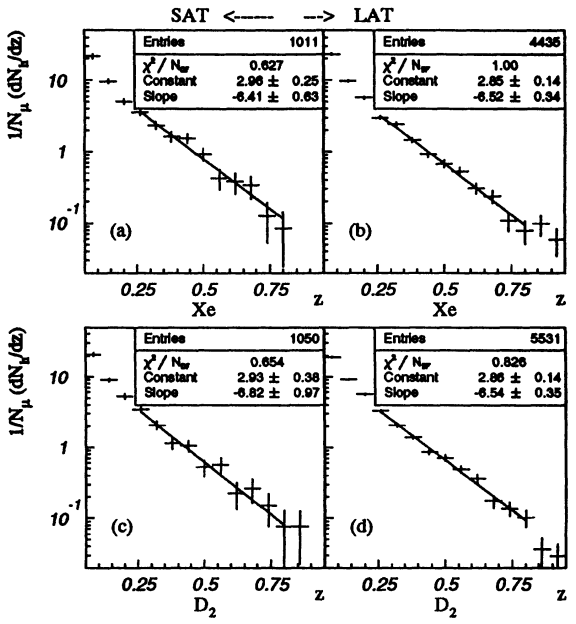

FIG. 36. z distributions for trigger overlap. These plots show the distributions for all charged particles; those from the SAT trigger are on the left, while those from the LAT trigger are on the right. The distribution from xenon SAT is in (a) and that from xenon LAT in (b); the distributions from deuterium SAT and LAT are in (c) and (d), respectively. These data have been corrected for acceptance.

a. Merging SAT and LAT

We investigated the justification for merging the data from the SAT and LAT trigger samples. Although the acceptance of the LAT should be a subset of the SAT, the phase space of the muon beam for the SAT was only 12% of that of the LAT.

The events which satisfied both the LAT and the SAT triggers were removed from the LAT samples of deuterium and xenon, but left in the SAT samples. Of these 3235 events in deuterium, only 1725 passed the kinematic and diffractive-removal cuts, and 1611 survived the calorimeter cuts. There were 2966 original events in xenon; 1258 survived the kinematic cuts, and 1089 survived the calorimeter cuts.

In order to compare the trigger samples, we chose events with the same basic kinematic qualities, using the *kinematic overlap* region defined by Eq. (A2). Both trigger samples had enough events in this region to provide a valid comparison, and these numbers of events are shown in Table XIII.

The possible effects of the two triggers on the hadron distributions were of primary interest. The z distributions are plotted in Fig. 36, with those from the SAT samples on the left and those from the LAT sample on the right. The xenon samples are on the top, and the deuterium samples are on the bottom.

Each distribution has been fitted to an exponential

TABLE XIII. Kinematic overlap samples. The first four lines indicate the numbers of events of the four samples which satisfied the kinematic constraints of the overlap region. The last two lines indicate the number of events in this overlap region which satisfied both triggers SAT and LAT; these events were included in the SAT samples.

Sample	Number of events
D2 SAT	583
D2 LAT	3014
Xe SAT	565
Xe LAT	2413
D2 LAT/SAT	401
Xe LAT/SAT	247

function of the form of Eq. (25). Comparing the parameters of these fits between distributions is a concise method of comparing the distributions. Since these samples are restricted to lie in a region with comparable kinematics, they should belong to the same "parent" distributions. The similarity of the "constant" and "slope" parameters from the fits with their errors suggests that the distributions from the two trigger samples are consistent. Consequently, we expect no biasing of the hadronic final state distributions due to the merging of the samples from the SAT and the LAT triggers for each target.

APPENDIX B: TABULATED DATA

In this section we have tabulated the data of the physics results which are graphed throughout the paper. Each table lists the corresponding figure in which its data are plotted.

TABLE XIV. Shadowing in cross section ratios. These tables contain the ratios of cross sections $(\sigma_{Xe}/A_{Xe})/(\sigma_{D_2}/A_{D_2})$. The ratio is tabulated first as a function of x_{Bj}. Then, it is tabulated as a function of Q^2 $(\mathrm{GeV}/c)^2$, for a low-x_{Bj} range, defined by $0.001 < x_{Bj} < 0.025$, and for a high-x_{Bj} range, defined by $0.025 < x_{Bj} < 0.2$. The systematic uncertainty on these ratios is 6%. These data are graphed in Fig. 3.

			$(0.001 < x_{Bj} < 0.025)$			$(0.025 < x_{Bj} < 0.2)$		
x_{Bj}	Ratio	Error	Q^2	Ratio	Error	Q^2	Ratio	Error
0.0013	0.669	0.022	0.13	0.739	0.086	2.04	0.935	0.158
0.0021	0.734	0.027	0.21	0.856	0.050	3.47	1.004	0.084
0.0035	0.820	0.031	0.36	0.776	0.032	5.75	1.024	0.073
0.0060	0.860	0.033	0.59	0.747	0.025	9.77	1.000	0.076
0.0098	0.869	0.035	0.98	0.917	0.031	16.22	1.137	0.105
0.0160	0.928	0.043	1.62	0.918	0.035	27.54	0.918	0.126
0.0270	1.037	0.055	2.70	0.902	0.045	45.71	1.272	0.270
0.0450	1.032	0.065	4.50	0.796	0.050	77.62	0.653	0.217
0.0740	1.022	0.082	7.41	0.960	0.097			
0.1260	1.007	0.112	12.30	0.927	0.172			

TABLE XV. Q^2 distributions. This table contains the event distributions tabulated as functions of Q^2 $(\mathrm{GeV}/c)^2$, for both the low and the high ranges of kinematics, for both the deuterium and the xenon targets. These data are graphed in Figs. 4 and 5. The errors on the plots are simply the square roots of the entries in each bin.

Kin_1			Kin_2		
Q^2	Xe	D_2	Q^2	Xe	D_2
0.15	1	0	7.5	353	421
0.25	94	138	12.5	505	568
0.35	182	219	17.5	371	409
0.45	152	226	22.5	240	255
0.55	119	137	27.5	157	182
0.65	111	148	32.5	107	132
0.75	110	139	37.5	70	91
0.85	98	125	42.5	54	58
0.95	116	125	47.5	53	46
			52.5	32	51
			57.5	24	37
			62.5	21	17
			67.5	27	32
			72.5	14	16
			77.5	14	22
			82.5	10	9
			87.5	9	13
			92.5	9	4
			97.5	5	9
			102.5	2	5
			107.5	7	7
			112.5	3	5
			117.5	4	3
			122.5	2	4

TABLE XVI. ν distributions. This table contains the event distributions tabulated as functions of ν (GeV), for both the low and the high ranges of kinematics, for both the deuterium and the xenon targets. These data are graphed in Figs. 4 and 5. The errors on the plots are simply the square roots of the entries in each bin.

Kin_1			Kin_2		
ν	Xe	D_2	ν	Xe	D_2
110	265	335	110	498	552
130	211	277	130	375	399
150	168	198	150	276	301
170	118	155	170	209	244
190	89	112	190	163	185
210	61	87	210	129	147
230	46	67	230	94	115
250	19	17	250	89	114
270	4	7	270	74	100
290	2	2	290	66	58
			310	47	68
			330	40	62
			350	24	31
			370	14	18
			390	10	14
			410	3	4
			430	0	2
			450	1	1
			470	1	0
			490	0	1

TABLE XVII. x_{Bj} distributions. This table contains the event distributions tabulated as functions of x_{Bj}, for both the low and the high ranges of kinematics, for both the deuterium and the xenon targets. These data are graphed in Figs. 4 and 5. The errors on the plots are simply the square roots of the entries in each bin.

Kin_1			Kin_2		
x_{Bj}	Xe	D_2	x_{Bj}	Xe	D_2
			0.03	574	685
			0.05	594	716
			0.07	315	333
0.00112	178	235	0.09	208	203
0.00137	143	202	0.11	114	116
0.00162	123	154	0.13	76	80
0.00187	100	132	0.15	48	68
0.00212	70	97	0.17	52	49
0.00237	71	74	0.19	34	30
0.00262	55	77	0.21	19	37
0.00287	44	48	0.23	18	25
0.00312	51	69	0.25	10	11
0.00337	39	39	0.27	8	17
0.00362	32	37	0.29	9	11
0.00387	27	33	0.31	9	12
0.00412	27	25	0.33	9	6
0.00438	11	15	0.35	3	5
0.00463	9	14	0.37	3	3
0.00488	3	6	0.39	1	3
			0.41	3	2
			0.43	0	0
			0.45	1	0
			0.47	1	0
			0.49	1	0

TABLE XVIII. W^2 distributions. This table contains the event distributions tabulated as functions of W^2 (GeV^2), for both the low and the high ranges of kinematics, for both the deuterium and the xenon targets. These data are graphed in Figs. 4 and 5. The errors on the plots are simply the square roots of the entries in each bin.

Kin_1			Kin_2		
W^2	Xe	D_2	W^2	Xe	D_2
90			90	2	2
126			126	8	13
162			162	95	131
198	198	254	198	491	499
234	213	278	234	356	383
270	171	217	270	257	297
306	137	166	306	207	234
342	105	114	342	142	169
378	63	95	378	129	146
414	54	78	414	94	118
450	30	39	450	84	104
486	8	14	486	78	87
522	2	2	522	54	62
558	2	0	558	41	61
			594	31	55
			630	23	26
			666	10	15
			702	8	8
			738	1	3
			774	0	2
			810	1	0
			846	1	1

TABLE XIX. z distribution: xenon and deuterium, Kin_1 and Kin_2. These data are graphed in Fig. 7.

	Kin_1				Kin_2			
z	$D_{Xe}(z)$	σ_{Xe}	$D_{D_2}(z)$	σ_{D_2}	$D_{Xe}(z)$	σ_{Xe}	$D_{D_2}(z)$	σ_{D_2}
0.08	23.337	1.231	21.157	0.964	20.774	0.744	18.235	0.585
0.14	9.864	0.518	9.741	0.435	9.440	0.342	8.916	0.297
0.20	5.817	0.380	5.692	0.319	5.859	0.260	4.731	0.210
0.26	4.066	0.315	3.560	0.251	3.413	0.196	3.327	0.175
0.32	2.459	0.244	2.426	0.207	2.276	0.160	2.128	0.139
0.38	1.583	0.195	1.615	0.168	1.341	0.122	1.310	0.109
0.44	0.768	0.136	0.843	0.122	0.918	0.101	0.902	0.091
0.50	0.938	0.150	0.700	0.111	0.694	0.088	0.564	0.072
0.56	0.408	0.099	0.421	0.086	0.458	0.072	0.447	0.064
0.62	0.409	0.099	0.493	0.093	0.291	0.057	0.328	0.055
0.68	0.313	0.087	0.385	0.082	0.234	0.051	0.219	0.045
0.74	0.216	0.072	0.140	0.049	0.101	0.034	0.145	0.036
0.80	0.192	0.068	0.088	0.039	0.089	0.031	0.027	0.016
0.86	0.121	0.054	0.106	0.043	0.045	0.023	0.046	0.020
0.92	0.072	0.042	0.035	0.025	0.011	0.011	0.036	0.018

TABLE XX. Corrected z distribution: xenon and deuterium, Kin_1, Kin_2, and full kinematic range. These data have been corrected for target length effects. They are graphed in Fig. 13.

	Kin_1				Kin_2				Full Kinematic range			
z	D_{Xe}	σ_{Xe}	$D_{\mathrm{D}_2}(z)$	σ_{D_2}	$D_{\mathrm{Xe}}(z)$	σ_{Xe}	$D_{\mathrm{D}_2}(z)$	σ_{D_2}	$D_{\mathrm{Xe}}(z)$	σ_{Xe}	$D_{\mathrm{D}_2}(z)$	σ_{D_2}
0.08	23.337	1.231	21.157	0.964	20.774	0.744	18.235	0.585	21.800	0.358	20.439	0.309
0.14	9.864	0.518	9.741	0.435	9.440	0.342	8.916	0.297	9.649	0.168	9.834	0.156
0.20	5.817	0.380	5.692	0.319	5.859	0.260	4.731	0.210	5.692	0.125	5.668	0.115
0.26	4.066	0.315	3.560	0.251	3.413	0.196	3.327	0.175	3.228	0.093	3.564	0.090
0.32	2.459	0.244	2.426	0.207	2.276	0.160	2.128	0.139	2.257	0.078	2.323	0.073
0.38	1.583	0.195	1.615	0.168	1.341	0.122	1.310	0.109	1.469	0.063	1.504	0.058
0.44	0.768	0.136	0.843	0.122	0.918	0.101	0.902	0.091	0.904	0.049	1.020	0.048
0.50	0.938	0.150	0.700	0.111	0.694	0.088	0.564	0.072	0.747	0.045	0.755	0.041
0.56	0.408	0.099	0.421	0.086	0.458	0.072	0.447	0.064	0.443	0.034	0.466	0.032
0.62	0.409	0.099	0.493	0.093	0.291	0.057	0.328	0.055	0.299	0.028	0.360	0.029
0.68	0.313	0.087	0.385	0.082	0.234	0.051	0.219	0.045	0.285	0.028	0.257	0.024
0.74	0.216	0.072	0.140	0.049	0.101	0.034	0.145	0.036	0.146	0.020	0.146	0.018
0.80	0.192	0.068	0.088	0.039	0.089	0.031	0.027	0.016	0.112	0.017	0.086	0.014
0.86	0.121	0.054	0.106	0.043	0.045	0.023	0.046	0.020	0.080	0.015	0.070	0.013
0.92	0.072	0.042	0.035	0.025	0.011	0.011	0.036	0.018	0.043	0.011	0.045	0.010

TABLE XXI. z_1 distribution: xenon and deuterium, Kin_1 and Kin_2. These data are graphed in Fig. 16.

	Kin_1				Kin_2			
z_1	$D_{\mathrm{Xe}}(z)$	σ_{Xe}	$D_{\mathrm{D}_2}(z)$	σ_{D_2}	$D_{\mathrm{Xe}}(z)$	σ_{Xe}	$D_{\mathrm{D}_2}(z)$	σ_{D_2}
0.08	5.514	0.661	4.650	0.459	4.841	0.365	4.040	0.262
0.14	4.313	0.341	4.141	0.284	4.007	0.222	3.583	0.188
0.20	3.798	0.307	3.395	0.246	3.778	0.208	3.145	0.171
0.26	2.726	0.258	2.731	0.219	2.705	0.175	2.667	0.156
0.32	2.025	0.221	2.162	0.195	2.063	0.152	1.945	0.133
0.38	1.391	0.183	1.422	0.158	1.274	0.119	1.247	0.107
0.44	0.768	0.136	0.843	0.122	0.918	0.101	0.902	0.091
0.50	0.938	0.150	0.700	0.111	0.694	0.088	0.564	0.072
0.56	0.408	0.099	0.421	0.086	0.458	0.072	0.447	0.064
0.62	0.409	0.099	0.493	0.093	0.291	0.057	0.328	0.055
0.68	0.313	0.087	0.385	0.082	0.234	0.051	0.219	0.045
0.74	0.216	0.072	0.140	0.049	0.101	0.034	0.145	0.036
0.80	0.192	0.068	0.088	0.039	0.089	0.031	0.027	0.016
0.86	0.121	0.054	0.106	0.043	0.045	0.023	0.046	0.020
0.92	0.072	0.042	0.035	0.025	0.011	0.011	0.036	0.018

TABLE XXII. z_2 distribution: xenon and deuterium, Kin_1 and Kin_2. These data are graphed in Fig. 17.

	Kin_1				Kin_2			
z_2	$D_{\mathrm{Xe}}(z)$	σ_{Xe}	$D_{\mathrm{D}_2}(z)$	σ_{D_2}	$D_{\mathrm{Xe}}(z)$	σ_{Xe}	$D_{\mathrm{D}_2}(z)$	σ_{D_2}
0.07	9.045	0.894	9.258	0.874	9.164	0.678	7.794	0.526
0.11	6.673	0.555	5.529	0.425	5.497	0.338	5.102	0.287
0.15	3.121	0.352	4.175	0.344	3.409	0.249	3.689	0.230
0.19	2.021	0.275	2.427	0.256	2.163	0.194	1.520	0.146
0.23	1.398	0.227	1.170	0.176	1.055	0.134	0.871	0.110
0.27	1.093	0.200	0.608	0.127	0.673	0.106	0.603	0.091
0.31	0.507	0.136	0.238	0.079	0.185	0.056	0.234	0.057
0.35	0.179	0.080	0.263	0.083	0.135	0.048	0.082	0.033
0.39	0.252	0.095	0.184	0.070	0.084	0.037	0.055	0.027

TABLE XXIII. z_3 distribution: xenon and deuterium, Kin_1 and Kin_2. These data are graphed in Fig. 18.

	Kin_1				Kin_2			
z_3	$D_{\mathrm{Xe}}(z)$	σ_{Xe}	$D_{\mathrm{D}_2}(z)$	σ_{D_2}	$D_{\mathrm{Xe}}(z)$	σ_{Xe}	$D_{\mathrm{D}_2}(z)$	σ_{D_2}
0.063	7.873	1.178	7.872	0.924	6.697	0.644	6.394	0.585
0.090	5.433	0.696	3.997	0.462	4.316	0.396	3.430	0.307
0.117	1.847	0.351	2.031	0.304	1.859	0.239	2.144	0.222
0.143	0.887	0.230	0.688	0.172	1.300	0.188	0.831	0.135
0.170	0.919	0.230	0.330	0.117	0.555	0.121	0.358	0.087
0.197	0.165	0.095	0.360	0.120	0.132	0.059	0.186	0.062
0.223	0.166	0.096	0.159	0.079	0.101	0.050	0.124	0.051
0.250	0.000	0.000	0.040	0.040	0.026	0.026	0.000	0.000
0.277	0.000	0.000	0.000	0.000	0.000	0.000	0.021	0.021
0.303	0.000	0.000	0.000	0.000	0.025	0.025	0.000	0.000

TABLE XXIV. Rescaled-z_2 distribution: xenon and deuterium, Kin_1 and Kin_2. These data are graphed in Figs. 19 and 20.

	Kin_1				Kin_2			
Rescaled z_2	$D_{\mathrm{Xe}}(z)$	σ_{Xe}	$D_{\mathrm{D}_2}(z)$	σ_{D_2}	$D_{\mathrm{Xe}}(z)$	σ_{Xe}	$D_{\mathrm{D}_2}(z)$	σ_{D_2}
0.08	6.233	0.801	7.498	0.807	7.202	0.601	6.193	0.533
0.14	4.806	0.398	3.826	0.306	4.080	0.250	3.770	0.234
0.20	1.834	0.225	2.600	0.225	2.215	0.169	2.224	0.152
0.26	1.442	0.206	1.350	0.161	1.505	0.134	1.214	0.107
0.32	1.051	0.185	0.913	0.130	0.685	0.091	0.789	0.086
0.38	0.562	0.117	0.517	0.098	0.515	0.077	0.453	0.068
0.44	0.400	0.100	0.306	0.074	0.274	0.056	0.211	0.044
0.50	0.224	0.075	0.327	0.077	0.168	0.043	0.160	0.039
0.56	0.193	0.068	0.142	0.050	0.103	0.034	0.110	0.032
0.62	0.198	0.070	0.107	0.044	0.057	0.026	0.046	0.021
0.68	0.122	0.054	0.070	0.035	0.067	0.027	0.055	0.023
0.74	0.218	0.073	0.070	0.035	0.011	0.011	0.010	0.010
0.80	0.048	0.034	0.052	0.030	0.011	0.011	0.000	0.000
0.86	0.000	0.000	0.000	0.000	0.022	0.016	0.018	0.013
0.92	0.000	0.000	0.000	0.000	0.011	0.011	0.000	0.000

TABLE XXV. Rescaled-z_3 distribution: xenon and deuterium, Kin_1 and Kin_2. These data are graphed in Figs. 19 and 20.

	Kin_1				Kin_2			
Rescaled z_3	$D_{\mathrm{Xe}}(z)$	σ_{Xe}	$D_{\mathrm{D}_2}(z)$	σ_{D_2}	$D_{\mathrm{Xe}}(z)$	σ_{Xe}	$D_{\mathrm{D}_2}(z)$	σ_{D_2}
0.08	6.830	1.392	5.975	1.504	6.520	1.215	5.165	0.737
0.14	2.802	0.351	2.099	0.247	2.453	0.247	4.249	1.334
0.20	1.063	0.278	1.130	0.163	1.006	0.120	1.069	0.133
0.26	0.398	0.108	0.443	0.096	0.851	0.140	0.510	0.073
0.32	0.458	0.116	0.204	0.065	0.224	0.052	0.252	0.052
0.38	0.189	0.072	0.173	0.107	0.119	0.038	0.200	0.044
0.44	0.074	0.043	0.179	0.060	0.126	0.040	0.076	0.027
0.50	0.099	0.050	0.088	0.039	0.082	0.031	0.028	0.016
0.56	0.086	0.050	0.018	0.018	0.000	0.000	0.047	0.021
0.62	0.000	0.000	0.000	0.000	0.023	0.016	0.000	0.000
0.68	0.000	0.000	0.000	0.000	0.000	0.000	0.019	0.013
0.74	0.000	0.000	0.018	0.018	0.000	0.000	0.009	0.009
0.80	0.000	0.000	0.000	0.000	0.000	0.000	0.000	0.000
0.86	0.092	0.092	0.000	0.000	0.000	0.000	0.000	0.000
0.92	0.000	0.000	0.000	0.000	0.026	0.018	0.000	0.000

TABLE XXVI. Rescaled z, full kinematics. This table includes the data of the rescaled-z values for xenon and deuterium, including the full kinematic sample. These data are graphed in Fig. 22.

	z_1				Rescaled z_2				Rescaled z_3			
Rescaled z_j	$D_{\mathrm{Xe}}(z)$	σ_{Xe}	$D_{\mathrm{D}_2}(z)$	σ_{D_2}	$D_{\mathrm{Xe}}(z)$	σ_{Xe}	$D_{\mathrm{D}_2}(z)$	σ_{D_2}	$D_{\mathrm{Xe}}(z)$	σ_{Xe}	$D_{\mathrm{D}_2}(z)$	σ_{D_2}
0.08	4.957	0.166	4.228	0.132	7.189	0.426	6.716	0.344	7.174	0.590	6.112	0.490
0.14	4.093	0.107	3.900	0.091	4.169	0.127	3.744	0.108	2.574	0.180	2.585	0.303
0.20	3.570	0.097	3.298	0.082	2.204	0.087	2.229	0.076	1.200	0.104	1.043	0.053
0.26	2.440	0.080	2.525	0.071	1.316	0.061	1.293	0.053	0.520	0.045	0.529	0.037
0.32	1.955	0.071	1.861	0.061	0.783	0.047	0.762	0.040	0.265	0.028	0.243	0.024
0.38	1.353	0.059	1.251	0.050	0.423	0.034	0.448	0.031	0.153	0.021	0.185	0.023
0.44	0.881	0.048	0.901	0.043	0.326	0.029	0.259	0.023	0.074	0.015	0.094	0.014
0.50	0.722	0.043	0.672	0.037	0.182	0.022	0.164	0.018	0.057	0.012	0.049	0.010
0.56	0.433	0.034	0.415	0.029	0.111	0.017	0.133	0.016	0.036	0.010	0.042	0.009
0.62	0.292	0.028	0.321	0.025	0.082	0.015	0.074	0.012	0.025	0.008	0.008	0.004
0.68	0.279	0.027	0.229	0.021	0.079	0.014	0.068	0.012	0.016	0.007	0.027	0.009
0.74	0.143	0.019	0.130	0.016	0.042	0.010	0.030	0.008	0.017	0.007	0.016	0.006
0.80	0.109	0.017	0.076	0.012	0.026	0.008	0.016	0.006	0.008	0.005	0.011	0.005
0.86	0.078	0.014	0.062	0.011	0.010	0.005	0.004	0.003	0.013	0.010	0.002	0.002
0.92	0.042	0.010	0.040	0.009	0.005	0.004	0.004	0.003	0.009	0.005	0.002	0.002

TABLE XXVII. Rescaled z_j, $j \in \{1,2,3\}$, full kinematics. This table includes the data of the rescaled-z values for xenon and deuterium, where $j \in \{1,2,3\}$ indicates that the first three fastest particles are included in the samples. These data include the full kinematic sample; they are graphed in Fig. 23.

Rescaled z_j	$D_{\mathrm{Xe}}(z)$	σ_{Xe}	$D_{\mathrm{D_2}}(z)$	$\sigma_{\mathrm{D_2}}$
0.08	19.321	0.747	17.056	0.613
0.14	10.836	0.245	10.228	0.335
0.20	6.974	0.167	6.570	0.124
0.26	4.276	0.110	4.347	0.096
0.32	3.003	0.090	2.866	0.077
0.38	1.928	0.071	1.884	0.063
0.44	1.282	0.058	1.254	0.050
0.50	0.962	0.050	0.885	0.042
0.56	0.580	0.039	0.590	0.034
0.62	0.399	0.032	0.403	0.029
0.68	0.374	0.031	0.324	0.026
0.74	0.202	0.023	0.177	0.019
0.80	0.144	0.019	0.103	0.014
0.86	0.101	0.018	0.068	0.012
0.92	0.056	0.012	0.046	0.010

TABLE XXVIII. Monte Carlo z distributions. This table includes the distributions in z for a (LUND) Monte Carlo deuterium sample. These data are graphed in Fig. 24.

z_1	$D(z_1)$	σ_1	z_2	$D(z_2)$	σ_2	z_3	$D(z_3)$	σ_3
0.08	2.193	0.121	0.07	5.977	0.245	0.063	7.371	0.333
0.14	2.701	0.134	0.11	5.154	0.227	0.090	5.566	0.289
0.20	2.500	0.129	0.15	3.570	0.189	0.117	2.813	0.206
0.26	2.226	0.122	0.19	2.136	0.146	0.143	1.264	0.138
0.32	1.952	0.114	0.23	1.334	0.116	0.170	0.677	0.101
0.38	1.203	0.090	0.27	0.612	0.078	0.197	0.301	0.067
0.44	0.936	0.079	0.31	0.411	0.064	0.223	0.090	0.037
0.50	0.695	0.068	0.35	0.140	0.038	0.250	0.045	0.026
0.56	0.555	0.061	0.39	0.050	0.022	0.277	0.015	0.015
0.62	0.294	0.044	0.43	0.010	0.010	0.303	0.000	0.000
0.68	0.221	0.038	0.47	0.000	0.000	0.330	0.000	0.000
0.74	0.187	0.035	0.51	0.000	0.000	0.357	0.000	0.000
0.80	0.074	0.022	0.55	0.000	0.000	0.383	0.000	0.000
0.86	0.040	0.016	0.59	0.000	0.000	0.410	0.000	0.000
0.92	0.020	0.012	0.63	0.000	0.000	0.437	0.000	0.000

TABLE XXIX. Monte Carlo rescaled-z distributions. This table includes the distributions in the rescaled-z values for a (LUND) Monte Carlo deuterium sample. These data are graphed in Fig. 24.

Rescaled z_j	Rescaled z_2		Rescaled z_3	
	$D(z)$	σ_2	$D(z)$	σ_3
0.08	4.112	0.166	4.586	0.175
0.14	3.476	0.152	2.768	0.136
0.20	2.380	0.126	1.651	0.105
0.26	1.484	0.100	0.729	0.070
0.32	0.882	0.077	0.515	0.059
0.38	0.582	0.062	0.194	0.036
0.44	0.361	0.049	0.181	0.035
0.50	0.214	0.038	0.060	0.020
0.56	0.167	0.033	0.074	0.022
0.62	0.047	0.018	0.040	0.016
0.68	0.060	0.020	0.027	0.013
0.74	0.033	0.015	0.027	0.013
0.80	0.033	0.015	0.020	0.012
0.86	0.027	0.013	0.007	0.007
0.92	0.020	0.012	0.013	0.009

TABLE XXX. Ratios of z distributions: Xe/D_2. The ratios are labeled as $Xe/D_2(1)$, which stands for the ratio $D_{Xe}(z)/D_{D_2}(z)$ for Kin_1, and as $Xe/D_2(2)$, which stands for the ratio for Kin_2. These data are graphed in Fig. 7.

z	$Xe/D_2(1)$	σ_1	$Xe/D_2(2)$	σ_2
0.14	1.066	0.050	1.131	0.036
0.32	1.067	0.078	1.039	0.056
0.50	1.076	0.153	1.082	0.109
0.68	0.922	0.191	0.904	0.159
0.86	1.686	0.630	1.329	0.532

TABLE XXXI. Ratios of z distributions: Kin_1 / Kin_2. The ratios are labeled as Xe and D_2, which stands for the ratios of Kin_1 over Kin_2 for each target. These data are graphed in Fig. 8.

z	Xe	σ	D_2	σ
0.14	1.082	0.046	1.148	0.043
0.32	1.153	0.078	1.124	0.068
0.50	1.021	0.132	1.027	0.120
0.68	1.499	0.313	1.470	0.256
0.86	2.663	0.994	2.098	0.840

TABLE XXXII. Ratios of z distributions: Xe/D_2, corrected. The ratios are labeled as $Xe/D_2(1)$, which stands for the ratio $D_{Xe}(z)/D_{D_2}(z)$ for Kin_1, and as $Xe/D_2(2)$, which stands for the ratio for Kin_2, and as $Xe/D_2(F)$ for the full kinematic range. These ratios use the distributions which have been corrected for target length effects. These data are graphed in Fig. 13.

z	$Xe/D_2(1)$	σ_1	$Xe/D_2(2)$	σ_2	$Xe/D_2(F)$	σ_F
0.14	1.010	0.048	1.071	0.035	1.033	0.016
0.32	0.979	0.072	0.953	0.052	0.941	0.025
0.50	0.983	0.140	0.988	0.100	0.934	0.045
0.68	0.840	0.174	0.824	0.145	0.956	0.078
0.86	1.536	0.574	1.210	0.485	1.168	0.176

TABLE XXXIII. Ratios of z distributions: Xe/D_2, half-target. The ratios are labeled as $Xe/D_2(1)$, which stands for the ratio $D_{Xe}(z)/D_{D_2}(z)$ for Kin_1, and as $Xe/D_2(2)$, which stands for the ratio for Kin_2. These ratios use the distributions from only the downstream halves of each target.

z	$Xe/D_2(1)$	σ_1	$Xe/D_2(2)$	σ_2
0.14	1.046	0.068	1.161	0.052
0.32	1.070	0.109	0.962	0.073
0.50	1.123	0.227	1.035	0.142
0.68	0.768	0.215	1.052	0.265
0.86	1.045	0.527	3.110	2.106

TABLE XXXIV. Ratios of z distributions: Kin_1 / Kin_2, corrected. The ratios are labeled as Xe and D_2, which stands for the ratios of Kin_1 over Kin_2 for each target, using the distributions which have been corrected for target length effects. These data are graphed in Fig. 14.

z	Xe	σ	D_2	σ
0.14	1.081	0.047	1.147	0.045
0.32	1.153	0.078	1.122	0.069
0.50	1.021	0.132	1.025	0.120
0.68	1.499	0.313	1.470	0.256
0.86	2.663	0.994	2.098	0.840

TABLE XXXV. Ratios of z_1 distributions: Xe/D_2. The ratios are labeled as $Xe/D_2(1)$, which stands for the ratio $D_{Xe}(z)/D_{D_2}(z)$ for Kin_1, and as $Xe/D_2(2)$, which stands for the ratio for Kin_2. These data are graphed in Fig. 16.

z_1	$Xe/D_2(1)$	σ_1	$Xe/D_2(2)$	σ_2
0.14	1.118	0.086	1.173	0.059
0.32	0.973	0.080	1.031	0.060
0.50	1.076	0.153	1.082	0.109
0.68	0.922	0.191	0.904	0.159
0.86	1.686	0.630	1.329	0.532

TABLE XXXVI. Ratios of z_2 distributions: Xe/D_2. The ratios are labeled as $Xe/D_2(1)$, which stands for the ratio $D_{Xe}(z)/D_{D_2}(z)$ for Kin_1, and as $Xe/D_2(2)$, which stands for the ratio for Kin_2. These data are graphed in Fig. 17.

z_2	$Xe/D_2(1)$	σ_1	$Xe/D_2(2)$	σ_2
0.110	0.994	0.080	1.090	0.064
0.230	1.073	0.130	1.300	0.124
0.350	1.370	0.380	1.090	0.306

TABLE XXXVII. Ratios of z_3 distributions: Xe/D_2. The ratios are labeled as $Xe/D_2(1)$, which stands for the ratio $D_{Xe}(z)/D_{D_2}(z)$ for Kin_1, and as $Xe/D_2(2)$, which stands for the ratio for Kin_2. These data are graphed in Fig. 18.

z_3	$Xe/D_2(1)$	σ_1	$Xe/D_2(2)$	σ_2
0.090	1.090	0.132	1.076	0.091
0.170	1.431	0.350	1.445	0.247
0.250	0.839	0.613	0.872	0.511

TABLE XXXVIII. Ratios of rescaled-z_2 distributions: Xe/D_2. The ratios are labeled as $Xe/D_2(1)$, which stands for the ratio $D_{Xe}(z)/D_{D_2}(z)$ for Kin_1, and as $Xe/D_2(2)$, which stands for the ratio for Kin_2. These data are graphed in Fig. 21.

Rescaled z_2	$Xe/D_2(1)$	σ_1	$Xe/D_2(2)$	σ_2
0.140	0.924	0.089	1.108	0.078
0.320	1.099	0.141	1.101	0.100
0.500	1.054	0.245	1.134	0.227
0.680	2.171	0.742	1.222	0.499
0.860	0.926	0.846	2.413	2.090

TABLE XXXIX. Ratios of rescaled-z_3 distributions: Xe/D_2. The ratios are labeled as $Xe/D_2(1)$, which stands for the ratio $D_{Xe}(z)/D_{D_2}(z)$ for Kin_1, and as $Xe/D_2(2)$, which stands for the ratio for Kin_2. These data are graphed in Fig. 21.

Rescaled z_3	$Xe/D_2(1)$	σ_1	$Xe/D_2(2)$	σ_2
0.140	1.162	0.250	0.952	0.183
0.320	1.275	0.325	1.242	0.205
0.500	0.908	0.373	1.374	0.480
0.680	0.000	0.000	0.801	0.731

[1] M. R. Adams *et al.*, Nucl. Instrum. Methods **A291**, 533 (1990).
[2] (a) J. J. Ryan, Ph.D. thesis, Massachusetts Institute of Technology, Cambridge, MA, 1991; (b) see pp. 114–122.
[3] J. J. Aubert *et al.*, in *High Energy Physics—1980*, Proceedings of the 20th International Conference, Madison, Wisconsin, edited by L. Durand and L. Pondrom, AIP Conf. Proc. No. 68 (AIP, New York, 1981).
[4] W. A. Loomis *et al.*, Phys. Rev. D **19**, 2543 (1979).
[5] M. Arneodo *et al.*, Phys. Lett. B **211**, 493 (1988).
[6] M. R. Adams *et al.*, Phys. Lett. B **287**, 375 (1992).
[7] W. Busza, Acta Phys. Pol. B **8**, 333 (1977).
[8] T. Bauer, R. Spital, D. Yennie, and F. Pipkin, Rev. Mod. Phys. **50**, 261 (1978).
[9] M. R. Adams *et al.*, Z. Phys. C **61**, 179 (1994).
[10] T. Sjöstrand, Comput. Phys. Comm. **27**, 243 (1982).
[11] G. Kane, *Modern Elementary Particle Physics* (Addison-Wesley, Reading, MA, 1987).
[12] R. Field and R. Feynman, Nucl. Phys. **B136**, 1 (1978).
[13] J. J. Aubert *et al.*, Phys. Lett. **123B**, 275 (1983).
[14] G. Altarelli and G. Parisi, Nucl. Phys. **B126**, 298 (1977).
[15] V. Gribov and L. Lipatov, Yad. Fiz. **15**, 781 (1972) [Sov. J. Nucl. Phys. **15**, 438 (1972)].
[16] F. E. Close, J. Qiu, and R. G. Roberts, Phys. Rev. D **40**, 2820 (1989).
[17] A. H. Mueller, Phys. Rev. D **18**, 3705 (1978).
[18] S. Gupta and A. H. Mueller, Phys. Rev. D **20**, 118 (1979).
[19] J. D. Bjorken, Fermilab Technical Report No. PUB-86/16 (unpublished).
[20] W. Kittel, Acta Phys. Pol. B **12**, 1093 (1981).
[21] D. S. Barton *et al.*, Phys. Rev. D **27**, 2580 (1983).
[22] A. S. Carroll *et al.*, Phys. Lett. **80B**, 319 (1979).
[23] (a) R. Field and R. Feynman, Phys. Rev. D **15**, 2590 (1977); (b) see p. 2595.
[24] A. Bialas and M. Gyulassy, Nucl. Phys. **B291**, 793 (1987).
[25] G. V. Davidenko and N. N. Nikolaev, Nucl. Phys. **B135**, 333 (1978).
[26] A. Bialas and E. Bialas, Phys. Rev. D **21**, 675 (1980).
[27] M. R. Adams *et al.*, Phys. Rev. Lett. **68**, 3266 (1992).
[28] C. S. Tao, Ph.D. thesis, Harvard University, 1979.
[29] M. R. Adams *et al.*, Phys. Lett. **272B**, 163 (1991).
[30] P. M. Morse and H. Feshbach, in *Methods of Theoretical Physics* (McGraw-Hill, New York, 1953), Vol. I, Chap. 8.
[31] J. J. Ryan, Nucl. Instrum. Methods A **336**, 552 (1993).
[32] (a) M. A. Preston and R. K. Bhaduri, *Structure of the Nucleus* (Addison-Wesley, Reading, MA, 1975); (b) see p. 247; (c) see p. 102.
[33] R. Feynman, R. Field, and G. Fox, Phys. Rev. D **18**, 3320 (1978).
[34] L. S. Osborne *et al.*, Phys. Rev. Lett. **40**, 1624 (1978).
[35] J. J. Aubert *et al.*, Z. Phys. C **18**, 189 (1983).
[36] S. Aïd *et al.*, Fermilab E665 Internal Report No. SW142 (unpublished).
[37] C. Yamaguchi, T. Shintomi, and M. Masuda, Nucl. Instrum. Methods **106**, 471 (1973).
[38] J. Engler *et al.*, Nucl. Instrum. Methods **106**, 189 (1973).
[39] J. Bailey *et al.*, Nucl. Phys. **B106**, 385 (1976).